Choroid Plexus Hosts the Earliest Detectable Circadian Clock in the Brain

Hélène Vitet [1], Vuong Hung Truong [1], Jihwan Myung [1,2,*]

[1] Laboratory of Braintime, Graduate Institute of Mind, Brain and Consciousness (GIMBC), Taipei Medical University, New Taipei City 235, Taiwan
[2] Graduate Institute of Medical Sciences (GIMS), College of Medicine, Taipei Medical University, Taipei 110, Taiwan

[*] Correspondence: Jihwan Myung (jihwan@tmu.edu.tw)

Abstract

Embryonic circadian rhythms support normal development, and maternal chronodisruption is linked to miscarriages and neurodevelopmental risks, yet the identity of the earliest brain circadian oscillator and the mechanisms governing its emergence remain unknown. Using bioluminescent reporters for *Per2* and *Bmal1*, we identified the developmental window in which autonomous ~24 h oscillations first appear *ex vivo*. Contrary to the prevailing view that places the suprachiasmatic nucleus (SCN) as the earliest circadian structure at E14.5–E15.5, we found that the fourth ventricle choroid plexus (4VCP) exhibits PER2::LUC oscillations by E11.5–E12.5. Transcriptional profiling revealed significant phase shifts in multiple clock genes between E11.5 and E13.5, indicating a transition away from maternal synchrony and the onset of a differentiation program. Detailed characterization of these early oscillations showed hallmarks consistent with a saddle-node on an invariant circle (SNIC) bifurcation. Our findings identify the 4VCP as the earliest detectable brain circadian oscillator and clarify the process leading to the onset of the embryonic circadian clock in the brain. These results provide insights into maternal and fetal clock interactions during development, with implications for neonatal care.

Keywords: circadian clocks, choroid plexus, embryonic development, SNIC bifurcation, clock emergence, maternal synchrony

Graphical Abstract:

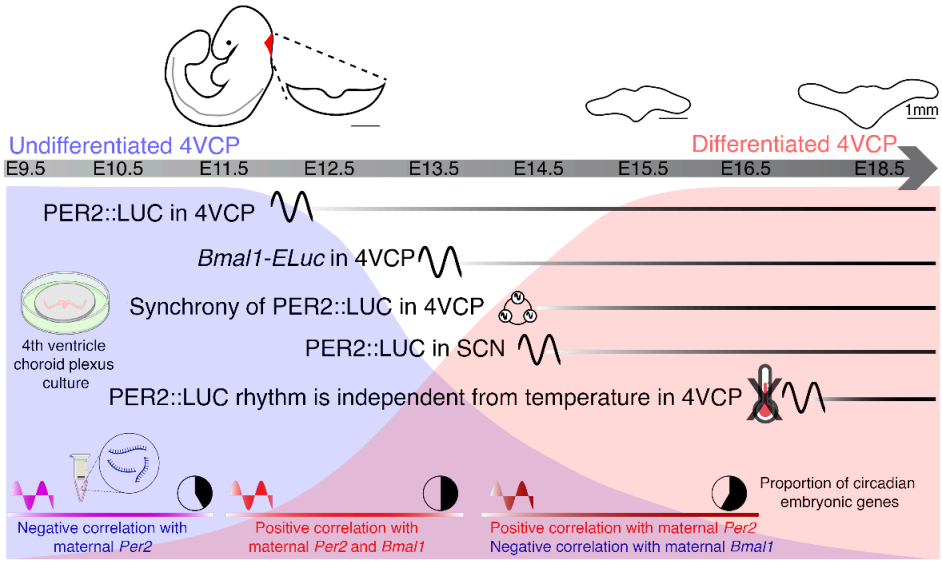

Timeline of 4VCP clock emergence before the SCN. In the embryonic 4VCP, PER2::LUC oscillations appear at E11.5–E12.5, and cellular synchrony increases abruptly around E14.5. *Bmal1-ELuc* oscillations appear at E13.5. The 4VCP entrains to a 0.5 °C temperature cycle through E16 but not at E18. The lower pie charts and gradients summarize the fraction of embryonic clock genes that are circadian and their correlation with maternal *Bmal1*, *Dbp*, and *Per2* expression.

Introduction

Circadian clocks are fundamental pacemakers that align physiology with Earth's 24 h cycle. Many physiological processes occur within a circadian timescale autonomously maintained by the transcription-translation feedback loop (TTFL). In this loop, the positive feedback component BMAL1:CLOCK activates transcription of the core negative feedback components such as *Per* and *Cry*, and the resulting PER:CRY complexes accumulate with a delay before repressing their own transcription upon nuclear translocation. While most mammalian tissues express circadian clocks, the suprachiasmatic nucleus (SCN) in the hypothalamus acts as the central clock, synchronizing other clocks throughout the body. Although mature circadian systems are increasingly well characterized, the timing and locus of the emergence of circadian rhythms during development remain poorly defined.

When? Circadian rhythms have been observed in prenatal stages in humans, non-human primates, and rodents (Maeda et al., 2006; Serón-Ferré et al., 2012; Landgraf et al., 2014). However, detecting embryonic clocks presents technical challenges, as experimental findings are often inconsistent due to low-amplitude oscillations and tissue-specific differences in clock gene expression. Although *Per* and *Bmal1* did not show clear rhythms when measured in whole-embryo *ex vivo* preparations (E10 to E17) (Cao et al., 2022; Dolatshad et al., 2010; Serón-Ferré et al., 2012), circadian rhythmicity of PER2 has been detected in the SCN *ex vivo* around E14.5 to E15.5 (Wreschnig et al., 2014; Carmona-Alcocer et al., 2018) and around E18 in peripheral organs such as the kidney (Dan et al., 2020), the heart (Umemura et al., 2017), and the liver (Dolatshad et al., 2010).

Embryonic brain morphogenesis depends on a complex interplay between the neural tube and the cerebrospinal fluid (CSF) pressure gradients. The dynamic homeostasis of CSF, produced primarily by the choroid plexus (CP), must be tightly regulated during this process. This non-neuronal tissue performs two roles: the CP epithelium filters the blood through its epithelial cells to produce CSF, acting as a gatekeeper at the fluid boundary of the brain, and it releases signaling molecules (5-HT, miRNAs) as well as peptides and proteins (TTR, cytokines, IGF2) into the CSF to support processes such as metabolism and signal transduction (Saunders et al., 2023; Chau et al., 2015; Courtney et al., 2025; Edelbo et al., 2023). In the embryo, the onset timing of CP epithelial CSF production remains unclear, in part because early in development the CP is not the only structure that shapes CSF composition (Bueno et al., 2020; Parvas et al., 2008). CSF is present as early as neural tube closure at E9.5, initially derived from the enclosed amniotic fluid. Its composition then transitions to CP-produced fluid between E10.5 and E14.5, coinciding with CP formation (Chau et al., 2015).

Where? Little is known about the exact locus in the brain where the earliest circadian clock emerges. Using bioluminescent reporters of circadian gene expression, PER2::LUC and

Bmal1-ELuc, we scanned *ex vivo* brain slices for circadian oscillations and monitored tissue explants collected from E9.5 onward throughout embryogenesis. This screening identified the 4VCP as the earliest locus with detectable circadian clock oscillations. We recently found that, in adult mice, the CP acts as a strong clock, as indicated by the persistence and amplitude of PER2::LUC reporter oscillations and by its ability to entrain the SCN (Myung et al., 2018). The CP is present in each of the brain ventricles, which are filled with the CSF. The lateral ventricle CP (LVCP) is contiguous with the third ventricle CP (3VCP) and separate from the fourth ventricle CP (4VCP) in the hindbrain. Differences among CPs include their developmental timelines and transcriptomes (Saunders et al., 2023; Lun et al., 2015a; Dziegielewska et al., 2001). In mice, the 4VCP develops first, followed by the LVCP (Lun et al., 2015b). Arising from the lower rhombic lip, between the roof plate and dorsal neuroepithelium, 4VCP development begins as early as E9.5, when it expresses *Wnt1*, transthyretin (*Ttr*), and potassium voltage-gated channel subfamily E member 2 (*Kcne2*). Development peaks between E11 and E12.5 (Lun et al., 2015b; Hunter and Dymecki, 2007), after which the 4VCP becomes anatomically apparent and is thought to be complete by E14, although proliferation continues postnatally (Lun et al., 2015b). At this stage, 4VCP cells are mature and express *Ttr, Otx2,* and *Wnt5a*, among other genes.

Embryonic CSF is crucial for the survival, proliferation, and differentiation of neural progenitors (Miyan et al., 2003; Martin et al., 2009; Gato et al., 2005; Parada et al., 2008; Alonso et al., 2011 and 2017; Huang et al., 2009) by delivering peptides and molecules, such as morphogens (retinoic acid, Sonic Hedgehog) and growth or trophic factors, such as FGF2 (Martin et al., 2006), EGF (Birecree et al., 1991), and IGF (Zappaterra and Lehtinen, 2012). CSF is also known for its role in shaping the brain through pressure against neuroepithelial walls (Gato and Desmond, 2009). The strong clock in the CP is thought to regulate this CSF secretome, which is sensitive to time of day (Edelbo et al., 2023). Very recently, apocrine secretion from the CP to the CSF has been identified as a mechanism that stimulates neuronal progenitor activity and modifies offspring behavior (Courtney et al., 2025). However, the embryonic CP clock remains poorly characterized, although it could modulate the temporal composition of CSF and, consequently, neurogenesis.

How? Circadian clocks are present across many mammalian cell types (Yamazaki et al., 2000; Yoo et al., 2004), yet the locus-specific sequence of their emergence in the brain suggests a programmed onset of circadian oscillations (Wreschnig et al., 2014; Carmona-Alcocer et al., 2018). Developmentally, the early embryo operates on distinct timescales, with cell divisions occurring on the order of hours before lengthening during neurogenesis, and somitogenesis proceeding on a short timescale of hours (Caviness et al., 1995; Oates et al., 2012). These rhythms may not synchronize well with the circadian clock, especially as the cell division timescale changes gradually. An abrupt transition between the somitogenesis era and the

circadian era has been proposed (Yagita *et al*., 2024), making the sudden emergence of the circadian clock *in vivo* plausible.

In nonlinear dynamics, a stable equilibrium can transition to a stable oscillation through mechanisms called bifurcations (Strogatz, 2024). Several types of bifurcation are distinguished by how amplitude and period behave near threshold and by their robustness to perturbations. Many oscillating biological systems, including circadian oscillators, are described by a (supercritical) Hopf bifurcation, characterized by a gradual increase in oscillation amplitude while the period stays near 24 h. The Hopf-based oscillator often fits dynamics of circadian clocks, consistent with experimental and modeling work (Murayama et al., 2017; Battogtokh and Tyson, 2018). Similarly, adult sinoatrial node pacemaking is typically governed by Hopf-type mechanisms, whereas the developmental onset of the first heartbeat in zebrafish arises via a noisy saddle-node on an invariant circle (SNIC) bifurcation (Jia et al., 2023). The SNIC bifurcation, also called SNIPER, is characterized by the abrupt appearance of nonzero amplitude and an initially long period that shortens toward ~24 h. At the single-cell level in the 4VCP, we observe a step-like increase in amplitude at onset and progressive shortening of the period during embryonic development, hallmarks consistent with SNIC-type dynamics. This bifurcation has specific implications for maternal-fetal coupling. Near a SNIC threshold, slow dynamics make oscillation frequency highly sensitive to weak biases. Consequently, weak maternal cues can efficiently entrain the nascent CP clock and synchronize weakly coupled CP cells by common drive. We observed such behavior at E14 in *ex vivo* 4VCP explants subjected to low-amplitude rhythmic temperature cycles.

In this study, we pinpoint when circadian rhythms first emerge in the 4VCP, identifying it as the earliest detectable clock in the embryonic mouse brain. We find hallmarks consistent with a discrete appearance of the circadian clock, including SNIC-like bifurcation behaviors and abrupt synchronization over development. These results clarify the timing, locus, and onset dynamics of the brain's first clock that potentially governs fluid homeostasis. Our findings also suggest implications for maternal chronodisruption, including shift work, during early pregnancy that can elevate risks of miscarriages and preterm birth (Cai et al., 2019; Davari et al., 2018) and for circadian support in neonatal care settings such as the Neonatal Intensive Care Unit (NICU) where preterm infants often show impaired rhythmicity (Govindan et al., 2024).

Material and Methods

Mice

Homozygous PER2::LUC mice (B6.129S6-*Per2*^{tm1Jt}/J, RRID: IMSR_JAX:006852) and heterozygous *Bmal1-ELuc* mice (Nakajima et al., 2010; a gift from Daisuke Ono, Nagoya University), maintained on the C57BL/6J background, were crossed with wild-type C57BL/6J

animals to generate heterozygous PER2::LUC$^{+/-}$ or *Bmal1-ELuc*$^{+/-}$ embryos. The PER2::LUC fusion protein reporter tracks PER2 abundance through a luciferase reaction (Yoo et al., 2004). *Bmal1* transcriptional activity was monitored with the *Bmal1-ELuc* reporter, with the high baseline removed by Hodrick-Prescott filter-based detrending (Myung et al., 2012). In this study, we treat *Bmal1-ELuc* as a transcript-level proxy and PER2::LUC as a protein-level proxy, as its luciferase activity peaks several hours after *Per2* transcription (Myung et al., 2025). Female and male mice were maintained under equinox light-dark (LD) cycles (12 h light:12 h dark; lights on at 07:00 and off at 19:00), with light-dark schedules controlled by LocoBox software (Truong and Myung, 2023) and constant ambient temperature and humidity conditions (24.0 ± 1.8 °C; 50.2 ± 8.7% RH). Zeitgeber Time (ZT) 0 is defined as the light-on hour. For sampling at ZT14 and ZT20, we used a reversed dark-light (DL) cycle (lights on at 22:00 and off at 10:00) and validated that gene expression levels matched those under LD cycles at E13.5 (**fig. S1**). All animal protocols were reviewed and approved by the Institutional Animal Care and Use Committee (IACUC) of the Taipei Medical University Laboratory Animal Center (protocols LAC-2019-0430, LAC2022-0381, LAC2022-0477, LAC2023-0037, and LAC2023-0038).

Tissue isolation and explant culture

Direct dissection. Tissue culture and bioluminescence recording followed our previous protocols (Myung et al., 2018). Pregnant female mice were anesthetized with isoflurane and euthanized at defined Zeitgeber times, and brains and embryos were rapidly removed into ice-cold Hank's balanced salt solution (HBSS; Sigma-Aldrich), supplemented with penicillin-streptomycin (10,000 U/mL; Gibco) and HEPES (1 M, pH 7.4). Embryonic tissues were dissected after decapitation using forceps and a scalpel under a stereomicroscope. For E9.5, the prosencephalon (containing both the SCN and LVCP progenitors) and the rhombencephalon (containing the 4VCP progenitors) were collected. For E10.5–E12.5, the 4VCP was extracted from the inferior part of the hindbrain roof plate epithelium, i.e., the lower rhombic lip containing rhombomere 2-8, located between the otic vesicles and the posterior part of rhombomere 1 (Hunter and Dymecki, 2007). For the LVCP, the cortical midline was used as the landmark for the LVCP progenitors. After E12.5, the CP becomes clearly distinguishable, and its dissection is similar to that of the adult mouse. The precision of 4VCP isolation throughout development was validated by RT-qPCR (**fig. S2**). The SCN from E10.5 to E13.5 was dissected from the ventral hypothalamus between the two optic cups (developing eyes). After E13.5, the SCN and the optic chiasm become more distinct, and the dissection procedure is the same as in the adult. This protocol was also used to isolate maternal and embryonic tissues in ice-cold PBS for biomolecular experiments.

Placenta dissection. We separated the light pink outer layer of the placenta (maternal decidua, considered here as the maternal placenta) from the darker pink inner layer (junctional zone and labyrinth, considered here as the embryonic placenta). The loose junction between these two sides of the placenta allows dissection with tweezers.

Tissue slicing. Heads or brains of mouse embryos at E11.5, E13.5, or E15.5 were sliced *ex vivo* on a vibratome (VT1000S, Leica Biosystems). Tissue was briefly dipped in two successive baths of low-melting point agarose (2% w/v; CAS 9012-36-6) at 37 °C, then embedded in an agarose block, glued to the vibratome stage and immersed in ice-cold HBSS. Using a diamond blade (Delaware Diamond Knives) advancing at ~0.025 mm/s and maximum frequency, 300 µm-thick slices were made and transferred to a culture membrane.

Explant culture. Each explant was cultured on a culture membrane insert (PICM0RG50, Merck Millipore) in a 35-mm dish containing 1 mL DMEM (Sigma-Aldrich) supplemented with B-27 (Gibco) and 200 µM beetle luciferin (Promega). The dish lid was sealed with high-vacuum grease (Molykote, DuPont) to prevent evaporation and maintained at a constant temperature of 37 .00 ± 0.01 °C in a hybrid refrigerator-heater incubator (MIR-154-PA, PHCbi). Temperature was monitored by placing an iButton (DS1921L, Maxim Integrated) adjacent to the dishes.

iDISCO tissue clearing and immunofluorescence labeling

After culture, the membrane supporting the brain slices was cut out and cleared using the iDISCO protocol (https://idisco.info/idisco-protocol). Briefly, after fixation in 4% PFA, the slices were rinsed and incubated in PBS for 3 days, then dehydrated in MeOH/H_2O in micro glass vials with PTFE caps, followed by an overnight incubation in 66% DCM/33% MeOH. Samples were then washed and bleached in 5% H_2O_2 overnight, before being rehydrated in MeOH/H_2O. Immunolabeling was conducted in a 96-well plate, starting with permeabilization (1 day) and blocking (1 day) at 37 °C, followed by incubation with primary antibody TTR (AB_10723946; GTX85112, chicken, 1:500, Genetex) for 2 days at 37 °C. Slices were then washed and incubated with secondary antibody (anti-chicken Alexa Fluor 568; AB_175477; ab175477, goat, 1:1000, Abcam) for 2 days at 37 °C. Similar steps of wash and blocking were applied before consecutive incubations with LHX1 (AB_531784; 4F2-c, mouse, 1:500, DSHB) and anti-mouse CF350 (SAB4600222, goat, 1:1000, Sigma) as before. Slices were then transferred back to the micro glass vials to undergo final clearing, beginning with dehydration in MeOH/H_2O followed by a 3-h incubation in 66% DCM/33% MeOH at room temperature. Finally, two 15-min incubations in 100% DCM were performed before mounting the slices on glass slides. Dibenzyl ether (DBE) was added directly over the slices, confined under a coverslip, and sealed with nail polish. Slices were then imaged using a DM IL fluorescence microscope (Leica Microsystems).

Time-lapse bioluminescence luminometry and imaging

Bioluminescence luminometry. For luminometry, the overall bioluminescence from each sample was recorded every 15 min with an integration time window of 108 s per dish, using a 32-dish rotating wheel with four photon-counting photomultiplier tubes (PMTs) (LumiCycle 32,

Actimetrics), housed in a refrigerator-heater incubator for precise temperature control (MIR-154-PA, PHCbi). Temperature was recorded continuously throughout the experiment.

Bioluminescence imaging. Single-cell imaging was performed on a custom-built incubator-microscope system equipped with an Orca R2 cooled CCD camera (Hamamatsu) with water cooling, combined with a 4x, NA 0.16 objective (UPLXAPO, Olympus) coupled to a 0.35x reduction lens (U-TV0.35XC-2, Olympus) to increase photon collection from bioluminescence (Myung et al., 2024), with a stage-top incubator (INUG2-WELS, Tokai Hit). Binning was set to 4×4, and exposure time was 60 min. Images were acquired using Micro-Manager 1.4 (Vale Lab, UCSF) via the DCAM-API (Hamamatsu) driver.

Real-time quantitative PCR (RT-qPCR)

RNA Isolation, cDNA synthesis, and RT-qPCR. After dissection of the embryonic or maternal 4VCPs at ZT2, ZT8, ZT14, and ZT20, the samples were stored at −80 °C. Embryonic 4VCPs from one dam (3–11 embryos per litter) were pooled, and at least 2–3 litters per time point were used. RNA sampling and RT-qPCR methods followed our previous protocol (Myung et al., 2015). 300 μL of TRK lysis buffer containing 2% β-mercaptoethanol was added to each sample, followed by an equal volume of chloroform after intensive homogenization. After phase separation and ethanol addition, microcolumns from the ENZA MicroElute Total RNA Kit (Omega Bio-Tek) were used to collect total RNA, with a final elution volume of 21 μL in DEPC-treated water. After evaluating the RNA concentration, cDNA was synthesized from 0.5–1 μg of total RNA using SuperScript IV Reverse Transcriptase (Thermo Fisher Scientific) with oligo$(dT)_{20}$ primers. PowerUp SYBR Green Master Mix (Applied Biosystems) was added to the cDNA samples, and RT-qPCR was performed in technical triplicate on a QuantStudio 3 Real-Time PCR System (Thermo Fisher Scientific). Primer sequences tested and used are listed in **table S1**.

Normalization. *Gapdh*, *Actb* (*β-actin*), and *Rpl13a* served as internal controls for embryonic samples (Hildyard et al., 2022). G*apdh* and *Actb* were used for maternal samples. For embryonic samples, after exclusion of outliers (ROUT test, Q = 1%), the differentiation status of each gene was assessed as the relative abundance of mRNA at a given embryonic stage (n > 8) normalized to the maximum abundance observed between E9.5 and E16.5. For example, at E9.5:

$$RNA_{E9.5}\,(\%) = \frac{mean\,(RNA_{E9.5})}{max\,(RNA_{E9.5-E16.5})} \times 100 \qquad (1)$$

Spectral analysis of bioluminescent time series and time of emergence quantification

Preprocessing. Visualization and preprocessing, including periodogram and fast Fourier transform (FFT)-based spectral analysis, were performed on Mathematica 13 (Wolfram Research) using the custom `PMTAnalysis` package (http://sourceforge.net/projects/imaginganalysis). Before analysis, the first 6 h of each recording were truncated. All circadian periods of the bioluminescence oscillations were estimated using FFT, and amplitudes were quantified as the root mean square (RMS) of detrended oscillations over fixed analysis windows: nominally 7 days for luminometry and 4VCP imaging, and 4 days for whole-brain slice imaging. Because the first 6 h were removed, some recordings were slightly shorter than 7 days. For image analysis of brain slices or the 4VCP, a 2×2-pixel grid was applied to the time-lapse images after removal of outlier pixels, and each ROI's standard deviation, center of mass, and mean gray value were measured using ImageJ (NIH).

Circadian power. Using a sliding-window FFT (2-day for luminometry data and 3-day window for imaging data), the time-lapse bioluminescence signals from PER2::LUC or *Bmal1-ELuc* were decomposed into spectral power and visualized as spectrograms over time. After integrating the power within specific period bands, the circadian power was calculated as the ratio of the total power in the circadian range (24 ± 4 h) to the total power across the full period range (3–58 h) (**fig. S3**). This yielded a time series of percent circadian power, which quantifies how strongly a gene oscillates within the circadian band relative to other period bands. Finally, the overall circadian power was computed as the average of these window-wise circadian power values across the entire recording. Circadian power thus provides a metric that captures the robustness of the circadian rhythm and accounts for damping, period variability, and noise. For a perfect sinusoid in a 2-day window, the maximal circadian power reaches ~60%, whereas for transient, rapidly damped oscillations, it falls below 20% (**fig. S3**). The blank control (luciferase medium without tissue explant) showed a maximal circadian power of ~20% (n = 10) (**Fig. 2D**). For SCN and 4VCP explants, the half-maximal level of the fitted circadian power curve across development was ~30% (30.83 ± 2.36% and 31.28 ± 1.70%, respectively).

Emergence Time. For rigorous identification of the emergence time points of the PER2::LUC and *Bmal1-ELuc* circadian rhythms, we performed nonlinear curve fitting using a sigmoid function. Blank recordings were used to estimate baseline circadian power and to provide null data points prior to E9.5. We then defined the emergence time (T_e) as the time when one-half of the maximum circadian power was reached (eq. 2).

$$P(t) = \frac{A}{1+e^{-(t-T_e)/\tau}} + C_0 \qquad (2)$$

where $P(t)$ is the circadian power at time t (time of sampling for explant), A is the amplitude above baseline, T_e is the half-maximal emergence time, τ is the time constant (slope

parameter), and C_0 is the baseline determined from blank recordings, with maximal power given by $A + C_0$.

Circadian promoter motif analysis

To systematically quantify the occurrence of circadian regulatory motifs, we analyzed promoter-proximal regions of 12 core circadian genes from our qPCR panel (**table S1**). Promoter regions were defined as -3,000 bp immediately upstream and +2,000 bp downstream of the transcription start site (TSS) in the *Mus musculus* genome assembly GRCm39. Gene coordinates and strand orientation were retrieved from Ensembl via the REST API (https://rest.ensembl.org/). To ensure all windows were extracted in the transcriptional orientation, minus-strand loci were reverse-complemented, so that upstream and downstream were always defined relative to the direction of transcription.

We scanned these sequences for known transcription factor binding motifs relevant to circadian regulation, including canonical and variant E-boxes (CACGTG, CACGTT, CACGTA), D-boxes (TTATGAA, TTATGTA), REV-ERB/ROR response elements (RRE/RORE) (AGGTCA, GGGTCA, [A/U]GGTCA), glucocorticoid response elements (GREs) including canonical palindromic (AGAACA[ACGT]TGTTCT), *Per2*-specific variants ([AG]G[ACGT]TGT[TC]CT), as well as half-sites ([AG]G[TA]ACA, TGT[TC]CT), and cAMP response element (CRE) half-sites (CGTCA, TGACG). Motifs were represented either as exact sequences or regular expressions to capture degenerate variants. Both forward and reverse-complement strands were scanned. Motif hits were identified using regular expression search with lookahead to permit overlapping matches. To account for overlapping motifs (e.g., GRE palindromes overlapping half-sites), we applied a priority-based deduplication scheme in which full palindromic motifs were retained over partial half-sites, and canonical motifs were prioritized over variants. Motif density was expressed as the number of motifs per kilobase of sequence for each gene and region. These densities are visualized as normalized motif densities (**fig. S6A**).

Hierarchical clustering and spectral analysis of gene expression profiles

Hierarchical clustering. To ensure comparability across genes, expression levels were first normalized using the internal control genes, then standardized using Z-scores: for each gene, the mean normalized expression was subtracted from each time point, and the result was divided by the standard deviation across all time points. To explore temporal relationships between genes, we used hierarchical clustering as implemented in the `seaborn.clustermap` function (v0.11.2) in Python (v3.6.13). This function computes pairwise distances between gene expression profiles using the Pearson correlation r_{ij} as the distance metric between genes i and j. Clustering was performed using average linkage, and results were visualized as a cluster heat map with a dendrogram that represents the similarity

relationships among genes based on their temporal patterns. Average linkage distance $D(A, B)$ was calculated as:

$$D(A,\ B)\ =\ \frac{1}{m\,n}\sum_{i\in A}\sum_{j\in B} d(i,j) \qquad (3)$$

where m and n are the numbers of genes in clusters A and B, respectively, and $d(i,j)$ is the distance defined as (1 - r_{ij}) between genes i and j. To summarize clusters, we identified representative genes for each cluster. For a given cluster, we computed its centroid by averaging the Z-scored expression profiles of all member genes across time points. We then calculated the Pearson correlation between each gene in the cluster and the cluster centroid. The gene with the highest correlation to the centroid was designated as the representative gene for that cluster, as it best reflected the average temporal pattern of its cluster.

Synchrosqueezed continuous wavelet transform (SST-CWT). Circadian gene expression profiles in embryos are sparsely sampled, and conventional Fourier or continuous wavelet transforms (CWT) often yield broad, smeared power spectra when signals have non-stationary components. SST-CWT sharpens time-frequency estimates by reassigning CWT coefficients from a range of supporting frequencies to a more precise instantaneous frequency (Daubechies et al., 2011). We implemented SST-CWT using the `cwt_sst` function from the `ssqueezepy` library (v0.6.5; https://github.com/OverLordGoldDragon/ssqueezepy). Prior to analysis, normalized gene expression time series were detrended with a moving average filter to reduce baseline drift. The signal was then mirrored and extended to improve edge behavior during the wavelet transform. We used a Morlet wavelet and 90 voices per octave. Although SST-CWT yields an amplitude spectrum, we refer to it here as a “power spectrum” to align with common usage in circadian biology (the true power is the squared amplitude). From the SST-CWT output, we retained periods from 3 to 58 h and calculated circadian power at each time point using the same 24 ± 4 h band as in the PER2::LUC and *Bmal1-ELuc* spectral analysis. This definition enables direct comparison between bioluminescence and qPCR-derived rhythmicity.

Phase dynamics and visualization. We estimated instantaneous phase (radians) along ridges of the time-frequency representation. Instead of plotting phase alone, we generated phase-weighted spectrograms, which multiply SST-CWT amplitude by its corresponding phase angle to highlight dominant oscillatory components with phase context. To improve visual clarity, colormap normalization and adaptive contrast scaling were applied using the maximum absolute value of each map. An illustration of this approach using simulated data is shown in **fig. S6A**.

Circular phase plots. To track phase across development (E10.5, E12.5, E14.5, E16.5), we constructed circular phase plots based on the estimated instantaneous phase within the circadian range (20–28 h). For each embryonic cluster, the representative gene was plotted

clockwise in a phase plot resembling a conventional clock, with 0 rad positioned at 12 o'clock. Nonrepresentative genes from the same cluster were plotted with smaller, semi-transparent markers for comparison. The left semicircle was shaded to distinguish early vs late phases. Marker shape and color indicated cluster identity, and genes with circadian power ≥ 20% were outlined in black. To assess potential maternal-embryonic coordination, dual-radius phase plots were used: the inner ring showed embryonic cluster representatives, and the outer ring showed selected maternal genes. Maternal-embryonic pairs were connected with dotted lines when both exhibited circadian power ≥ 20% and their phase difference was < $\pi/2$ rad (≤ 6 h), indicating possible phase alignment.

Sliding-window correlation and network construction. To assess temporal coordination among maternal and embryonic genes, time series were padded by duplicating the first and last two points, and 5-timepoint sliding windows were applied. Pearson correlation matrices were computed for each window, generating a time-resolved sequence of correlations. Examples of dynamic correlation are shown in **fig. S6B**. Networks were built in `NetworkX` (v2.5.1), with genes as nodes and edges weighted by average correlation within a developmental period. Edge consistency across periods was shown with solid lines, and changes in correlation sign with dashed lines. For maternal-embryo networks, only the top 30% strongest correlations were highlighted; the remainder were rendered in semi-transparent gray.

Statistical Analysis

Data are reported as mean ± standard error of the mean (SEM) unless otherwise specified. Circular phases are presented as mean ± circular standard deviation (SD). For parametric curve fits, we report best fit estimate ± standard error (SE), obtained from the asymptotic covariance matrix of the nonlinear least-squares fit. Statistical comparisons used Student's *t*-test for two groups (**fig. S1**), one-way ANOVA with Tukey's post hoc test for multiple groups, or two-way ANOVA followed by Sidak's post hoc test for two groups evolving with time. Linear relationships used ordinary least-squares regression with coefficient of determination (R^2) as goodness of fit, and a two-sided *p* value. For nonlinear fits, model selection was guided by the Akaike Information Criterion (AIC) and the Bayesian Information Criterion (BIC). No data were excluded as outliers except for the following cases: spurious FFT-derived period estimates in nonperiodic time series, clear failures in RNA level values, and dispersed data points of the amplitude and the period of 4VCP ROIs, where outliers were identified using ROUT test (Q = 1%). All statistical analyses were performed in GraphPad Prism 9 and Mathematica 13.

Results

PER2::LUC circadian oscillations emerge in the 4VCP before the SCN

The embryonic SCN is widely recognized as the earliest reported brain region to exhibit a detectable circadian rhythm, which emerges between E14.5 and E15.5 (Wreschnig et al., 2014; Carmona-Alcocer et al., 2018). To determine whether the SCN clock is unique at this developmental stage, we prepared brain slices from E15.5 PER2::LUC$^{+/-}$ embryos and performed bioluminescence imaging for 5–7 days (**Fig. 1Aa**, **movie S1**). Spectral analysis revealed two consistent loci exhibiting ~24 h periods, circadian power exceeding 30% (see Materials and Methods), and high RMS amplitude (**fig. S4**). The ventral locus (white arrow) was LHX1-positive, confirming its identity as the SCN (VanDunk et al., 2011), whereas the posterior structure (red arrow) was TTR-positive, a known marker for the CP (Stauder et al., 1986) (**Fig. 1Cc**). When analysis was restricted to the SCN and 4VCP, a robust rhythm with a period between 20 and 28 h was detected, with circadian power of 59.4 ± 0.8% in the SCN and 40.4 ± 0.4% in the 4VCP (**Fig. 1Cd**). The pituitary gland also exhibited rhythmicity (46.9 ± 0.4%), but with a markedly lower RMS amplitude (10.2 ± 0.2 AU) compared to the SCN and 4VCP (15.9 ± 0.9, $p < 0.0001$ and 15.5 ± 0.5 AU, $p < 0.0001$, respectively) (**fig. S4**).

To test whether the 4VCP begins to oscillate before the SCN, we repeated the experiment at E13.5 (**Fig. 1D**, **movie S2**). We did not observe any circadian oscillations from ventral structures corresponding to SCN progenitors, consistent with previous reports (Wreschnig et al., 2014; Carmona-Alcocer et al., 2018) (**Fig. 1Db**, **Dd**). However, only the 4VCP (red arrow) exhibited a near-24-h rhythm with strong circadian power and high RMS amplitude (hypothalamus: 20.7 ± 0.1%, 4VCP: 30.0 ± 0.7%) (**Fig. 1Db**, **fig. S4**), which we confirmed after restricting the analysis to the 4VCP (**Fig. 1Dd**). At E11.5, no significant circadian rhythm was detected in the 4VCP region in brain slices (**Fig. 1E**, **movie S3**).

Because the 4VCP in a slice could still be influenced by neighboring tissues, we asked whether the rhythm observed in E13.5 could originate from an endogenous 4VCP clock. Therefore, we dissected E13.5 4VCPs and recorded their bioluminescence *ex vivo* for 7 days (**Fig. 1F**, **movie S4**). We found that the isolated 4VCP explant exhibited robust circadian rhythmicity at E13.5, with a mean circadian power of ~40%, well above the detection threshold determined from blank luciferase medium (Blk, < 20%) (**Fig. 1Fb**).

To pinpoint the time of clock emergence, we dissected 4VCPs from PER2::LUC embryos at embryonic stages beginning at E9.5, when the CSF compartment forms during neural tube closure (Chau et al., 2015), to postnatal stages. We recorded the 4VCP PER2::LUC bioluminescence from 110 embryos, with 3–11 embryos from at least 2–3 litters per stage, for 7 days using PMTs. The period, initially long and dispersed (27.50 ± 2.12 h at E9.5; $p < 0.0001$ with $n = 3$), converged toward 24 h by E11.5 (24.98 ± 0.54 h; $p > 0.1$ with $n = 11$), when the first detectable oscillations appeared and circadian power exceeded 20% (31.42 ± 1.90% at E11.5; $p < 0.0001$ with $n = 15$; vs. 18.01 ± 2.43% at E10.5; $p > 0.05$ with $n = 15$) (**Fig. 2A**,**C**). However, as seen in the head slice (**Fig. 1Ec**), these oscillations were weakly sustained, with low RMS

amplitude. At E12.5, the oscillations persisted for the full 7-day recording, and their amplitude increased further at E13.5. The rhythm became fully circadian at E15.5 (24.47 ± 0.60 h; n = 5), with high circadian power (50.96 ± 3.42%; n = 5) relative to the 2-day window ceiling (~60%) (**Fig. 2A,C,D**). We also used the *Bmal1-ELuc* reporter strain to characterize the molecular assembly of the embryonic circadian clock. *Bmal1-ELuc* oscillations with a ~24 h period were observed from E13.5 to E14.5, approximately 2 days after the emergence of PER2 oscillations (**Fig. 2B,C,D**).

From the sigmoidal fits to circadian power trajectories (see Materials and Methods), we estimated the emergence time T_e and found that PER2::LUC oscillations started to be circadian at E11.7 ± 0.14 *ex vivo*, whereas *Bmal1-ELuc* oscillations emerged at E13.52 ± 0.70 *ex vivo* (**Fig. 2D**). This result aligns with the sudden shift of the circadian power of PER2::LUC above 20% observed at E12.5 (**fig. S5**). Because the circadian clock and developmental programs are intertwined, we mapped the embryonic 4VCP's developmental trajectory by quantifying mRNA levels for stage-associated genes. For progenitor or stem cell markers, we measured *Nanog* (stem cells), *Gli3* (neuroepithelium), *Wnt1* (roof-plate and CP epithelium progenitors) (Awatramani et al., 2003; Hunter and Dymecki, 2007), and *Ki67* (proliferation). We compared these with differentiation markers *Aqp1*, *Wnt5a*, *Ttr*, and *Otx2,* which are upregulated as the 4VCP matures (Johansson et al., 2013; Lun et al., 2015b; Langford et al., 2020) (**Fig. 2E**). After normalizing each transcript to its peak abundance between E9.5 and E16.5, we observed that progenitor markers predominate from E9.5 to E12.5, whereas differentiation genes dominate thereafter (**Fig. 2E**). Sigmoidal fits estimated the progenitor half-minimum at E13.63 ± 0.79 and the differentiation half-maximum at E13.52 ± 0.20, marking a sharp transition that coincided with the *Bmal1-ELuc* T_e in the 4VCP (E13.52 ± 0.70), as anticipated from developmental maturation (Yagita et al., 2024). By contrast, PER2::LUC oscillations appear earlier and autonomously (E11.70 ± 0.14), and precede *Bmal1* and the differentiation switch, an order that is atypical for a canonical TTFL (**Fig. 2G**).

Finally, we compared the emergence time of PER2::LUC rhythms across the brain and peripheral organs in isolated explant culture. Among all tissues tested, the 4VCP was the first to become circadian, preceding the LVCP (E12.37 ± 0.19), which develops later than the 4VCP (Lun et al., 2015b), and the SCN (E14.21 ± 0.41), consistent with previous reports (Carmona-Alcocer et al., 2018). In the SCN, the period approached 24 h at E14.5 (24.47 ± 2.35 h, n = 7) and became fully circadian at E15.5 with high circadian power (44.56 ± 2.48%, n = 3). Peripheral organs emerged later in gestation and after the SCN (liver: E14.53 ± 0.61; kidney: E15.08 ± 0.33) (**Fig. 2F**,**G**).

Early-to-late circadian gene expression in the embryonic 4VCP

Because mRNA and protein levels can be uncoupled during development (Umemura et al., 2017), we assessed the emergence of circadian mRNA expression rhythms in the 4VCP. To

capture circadian variation, we sampled embryonic 4VCPs from 106 litters across E9–E16 at four circadian timepoints (ZT2, ZT8, ZT14, ZT20) each embryonic day and performed RT-qPCR. We first compared the overall mRNA levels of a specific gene set throughout development, and observed that at E9, the highest transcript levels were for *Rora, Clock, Cry1,* and *Chrono*, rather than *Bmal1* and *Per1/2/3* (**Fig. 3A**).

We then clustered the transcripts according to their full temporal expression profiles across development (**Fig. 3B**). Pairwise distances between expression profiles were computed using the Pearson correlation, followed by hierarchical clustering. Three clusters emerged with distinct onset patterns: Cluster 1 rises from E9.5, peaking at E14.5 and then declines thereafter (*Rora*, *Per2*, *Rorc* and *Chrono*); Cluster 2 shows a late onset around E13.5 (*Rev-erbβ, Clock*, *Per3*, *Dbp*, *Bmal1*, *Rev-erbα* and *Per1*); Cluster 3 remains near constant across embryonic days (*Cry2*). In a window from 3 kb upstream to 2 kb downstream of each transcription start site (TSS), we quantified the normalized density of motifs targeted by transcription factors that regulate clock genes (**fig. S6A**). These clusters do not strictly align with the promoter-motif architecture expected from TTFL logic (Ukai-Tadenuma et al., 2008; Takahashi, 2017). Notably, *Bmal1* and *Clock*, drivers of the E-box loop, fall into Cluster 2, and their baseline expression increases later than *Per2* (**Fig. 3A**), mirroring the onset-timing difference noted in *Bmal1-ELuc* and PER2::LUC reporter oscillations (**Fig. 2G**). Moreover, *Per1* and *Per2*, both with glucocorticoid and cAMP response elements (GREs and CREs, respectively) in their promoters that can reset the clock in the CP (Liška et al., 2021), fall into two different clusters. These observations point to the possibility that embryonic circadian gene expression in the 4VCP departs from a simple TTFL-based expectation.

We evaluated how circadian rhythms of each gene compared with the clusters, which are more influenced by baseline changes across development, by quantifying circadian power using SST-CWT analysis (Materials and Methods; **fig. S6B**, **S7**, **S8A**). We found no consistent association between rhythmic strength and baseline expression, owing to pronounced within-cluster heterogeneity. Cluster 1 shows *Per2* and *Rora* as circadian from E9 to E13, while *Rorc* and *Chrono* become circadian after E13.5. Most Cluster 2 genes become circadian around E16.5, except for *Clock*, which exhibits a strong circadian power from ~E10.5, and *Dbp*, whose power is below the threshold from ~E10.5 onward. Finally, the Cluster 3 gene *Cry2* appears circadian around E10.5 (**Fig. 3C**). To further validate our findings, we created phase-weighted power spectrograms of representative transcripts (red), which visualize changes in dominant period and power together with phase across cycles (**Fig. 3C**, lower panels). For several genes, including *Rora, Clock, Per2,* and *Rev-erbα*, we confirmed an initial circadian rhythm at E9–E10 (circadian power ≥ 30%), which became indistinct around E13–E14 (circadian power ~20%) and reemerged at E16, except for *Clock*, with an almost inverted phase (**Fig. 3C**; **fig. S7**, **S8A**).

To better understand the establishment of the molecular clock and the dynamics between clusters, we next compared the expression of the embryonic clock genes across development with the representative gene of each cluster (**Fig. 3D**; **fig. S6C**) and summarized the phase correlations in **Fig. 3E**. From these correlative heat maps, we identified clusters whose correlations remained stable over time (solid line) (**Fig. 3E**), with Cluster 1 and the claudins being strongly positively correlated (**Fig. 3D**) and other clusters showing correlations that varied over development. For the latter, three eras were apparent: E9–E11, E11–E13, and E13–E16. Although this division suits most genes, it is especially clear for the dynamics between Cluster 1 (containing *Per2*) and Cluster 3 (*Cry2*); while they are generally in-phase (positively correlated), they become antiphase (negatively correlated) between E11.5 and E13.5 (**Fig. 3D**; **fig. S8B**). A similar trend can be seen with Cluster 1 (*Rora*) and Cluster 2 (*Per1*) as well as with *Cry2* and the tight junctions (*Cldn2* and *Cldn11*) (**Fig. 3D**; **fig. S8B**). Finally, we studied the phase of expression to understand the origin of the change in correlation. Not only did the phase of Cluster 2 and Cluster 3 change between E10.5 and E12.5, but the phases within each cluster also became more homogeneous (**Fig. 3F**). By E16.5, we observed a cluster polarization, with most genes positively correlated and in-phase, whereas Cluster 3 and the tight junctions were negatively correlated and antiphase to the others (**Fig. 3E**, **3F**).

The absence of sustained PER2::LUC or *Bmal1-ELuc* rhythms in the embryonic 4VCP before E11.5–E12.5 *ex vivo*, despite *Rora, Per2, Clock*, and *Cry2* (among others) being circadian *in vivo*, suggests that the early circadian gene expression may depend on external inputs, such as maternal cues (Wong et al., 2022). We therefore compared the expression profiles of selected clock genes in the 4VCP of 102 dams with the 4VCP of PER2::LUC embryos. From hierarchical clustering, we identified four clusters of maternal clock genes, which largely align with the gene classes, except for Cluster 4, which contains both E-box- and RRE-driven genes: *Cry1* and *Bmal1* (**Fig. 4A**). Surprisingly, in the maternal 4VCP, *Bmal1* and *Per2* expression, initially antiphasic ($p < 0.0001$ at E10.5 ZT2), became in-phase at E12.5 ($p > 0.05$ at E12.5 ZT2), which may help explain *Per2* forming its own cluster (**Fig. 4A**, **4C**; **fig. S10A**). SST-CWT analysis and circadian power estimation for each maternal gene (**fig. S9**) showed that all genes exhibited strong circadian power (**Fig. 4B**; **fig. S9**).

To investigate how maternal signals might influence embryonic clock development, we examined temporal correlations between maternal and embryonic gene expression (**Fig. 4D**, **4E**). We compared maternal *Per2*, *Bmal1*, *Rorc* and *Dbp* with representative genes from each embryonic cluster (**Fig. 4D**; **fig. S10C**). Except for some maternal and embryonic genes that were found to be correlated from E9.5 to E16.5 (maternal *Rorc* and embryonic *Chrono*; maternal *Bmal1* and embryonic *Dbp*) (**fig. S10B**), we found that these correlations were not static but dynamically reorganized during development, revealing three distinct epochs that mirror the embryonic expression timeline, although less sharply defined. Before E11.5, when the embryonic clock is still immature, maternal *Per2* is largely uncorrelated with all the

embryonic genes targeted in our study. Around E11.5, cluster-specific patterns emerged: Clusters 2 and 3 became positively correlated with maternal *Per2,* which is also the case for Cluster 1 but from E13.5 onward (**Fig. 4C, 4E**; **fig. S10B**). At E11.5, the correlation with maternal *Rorc* became globally positive, suggesting that maternal *Rorc* or an associated pathway may help synchronize newly rhythmic components of the embryonic clock. This period might signify a major developmental phase transition, where the embryo's internal clock becomes more autonomous but still responsive to maternal signals. From E13.5 to E16.5, as most embryonic clusters acquired circadian rhythmicity, embryonic genes became negatively correlated with maternal *Bmal1*. Dual-radius phase plots further revealed a shift in maternal *Per2* and *Rorc* expression, while maternal *Bmal1* and *Dbp* remained relatively stable (**Fig. 4F**). This shift of maternal *Per2* phase occurred when maternal-embryonic correlation patterns reorganized, raising the possibility that a subset of maternal clock genes might undergo their own adjustments during this developmental window. Whether this reflects intrinsic maternal dynamics or embryo-evoked feedback remains to be determined.

Taken together, these results indicate that maternal and embryonic clocks are coordinated, especially at E9.5–E11.5 when embryonic Clusters 1 and 3 are strongly correlated, and that the maternal clock appears to undergo a transient reorganization during the E11.5–E13.5 epoch. Notably, this epoch coincides with the functional maturation of the placenta, when maternal nutrient and oxygen supply to the embryonic circulation begins (Elmore et al., 2022). To test whether placental maturation contributes to this change in clock dynamics, we separated embryonic and maternal placentas and recorded PER2::LUC and *Bmal1-ELuc* bioluminescence *ex vivo*. As reported previously (Čečmanová et al., 2019), the embryonic placenta lacked autonomous circadian oscillations, whereas the maternal placenta exhibited robust rhythms with a transient mid-gestational attenuation (**Fig. 4G**). In the maternal placenta, circadian power of PER2::LUC and *Bmal1-ELuc* oscillations showed a mid-gestational nadir of ~20–30% at E15.3 ± 0.4 and E15.6 ± 0.6, respectively, estimated from inverted Gaussian fits. This dip occurs during E13–E15 and coincides with the timing of increased activity of 11β-hydroxysteroid dehydrogenase type 2 (11β-HSD2) (E12.5-E16.5) (Salvante et al., 2017; Brown RW et al., 1996; Thompson et al., 2002), which inactivates glucocorticoids and is mainly active in the maternal placenta, suggesting a potential endocrine gating mechanism that shields the embryo from maternal influence (Astiz and Oster, 2021), although causality remains to be tested.

Temperature cycles can drive the embryonic 4VCP rhythmicity until E16.5

During pregnancy, the maternal core body temperature rhythm amplitude dampens to ~1 °C, and to ~0.5 °C from around mid-gestation (Smarr et al., 2016). Because maternal circadian temperature changes around E11.5 and nutrition supply shifts from histiotrophic (yolk

sac-based) to hemotrophic (blood-based), beginning at ~E10 and becoming fully functional by E12.5–E13.5 (Elmore et al., 2022), we hypothesized that small intrauterine temperature cycles could serve as a non-bloodborne driver of the nascent embryonic clock. By contrast, adult peripheral clocks *in vitro* require larger temperature cycles for entrainment (~4 °C, Brown et al., 2002; ~2.5 °C, Buhr et al., 2010; ~1.5 °C, Abraham et al., 2010), consistent with heat shock factor activation thresholds near ~2.5 °C (Brown and Rush, 1996; Buhr et al., 2010). If the embryonic 4VCP entrains to a 0.5 °C cycle, this would imply heightened phase sensitivity near onset, as expected for a system close to a SNIC threshold, rather than the higher-amplitude requirements typical of mature Hopf-type limit cycle oscillators.

We therefore tested temperature entrainment directly by recording PER2::LUC activity in cultured embryonic 4VCP explants. Since maternal body temperature at E6 varies between 37.5 °C and 37 °C (Wharfe et al., 2016), we applied 2 days at 37 °C followed by 12 days of a 37–37.5 °C (Δ0.5 °C) square-wave cycle with a 26-h period to E14, E16, and E18 4VCP and lung explants (**Fig. 5A**). At E14, 4VCP PER2 rhythms phase-locked to the 26-h temperature cycle (circular SD = 0.47 rad; n = 5); at E16, they entrained after a brief transient (circular SD = 0.70 rad; n = 4); and by E18, they showed strong resistance to entrainment (circular SD = 1.16 rad; n = 4) (**Fig. 5B**). Across all embryonic stages, the lung clock entrained to the temperature cycle, possibly reflecting its prolonged structural maturation that continues postnatally. We applied the same protocol to the LVCP and SCN and found that the SCN remained entrainable at E18, which is plausible given that the SCN network is still immature at this stage (Bedont and Blackshaw, 2015), but the LVCP, like the 4VCP, was not (**fig. S11A**, **table S2**). Together, these results indicate that small temperature cycles can influence the embryonic 4VCP through E16, whereas by E18, the oscillator exhibits reduced sensitivity to small temperature gradients and behaves more like a robust, limit cycle oscillator that maintains a stable rhythm under constant conditions.

Abrupt, SNIC-like onset and synchronization of clock emergence

A transition from a stable equilibrium to self-sustained oscillation is called a bifurcation. Single-cell circadian clocks are well described by robust limit cycles often modeled near a supercritical Hopf bifurcation, with amplitude that increases smoothly while the period remains near 24 h (Leloup and Goldbeter, 1999). By contrast, systems near a SNIC threshold show an abrupt appearance of finite-amplitude oscillations, with very long initial periods that shorten toward ~24 h and can also display pronounced phase sensitivity to weak perturbations (Ermentrout, 1996). The bifurcation type can be probed by tracking how amplitude and period change over development. In our single-cell-resolution PER2::LUC imaging data, we observe a sharply defined onset, with a long initial period and stepwise increase in single-cell amplitude (**Fig. 5C**), consistent with a SNIC-like onset near the birth of the circadian clock. Whole-tissue PER2::LUC luminometry likewise shows a long initial period (26.4 ± 4.3 h) that converges to ~24 h over development (24.3 ± 1.1 h at E17.5) (**Fig. 2B**). The apparent linear increase in

whole-tissue amplitude may partly reflect growth in 4VCP cell number across development (**fig. S11B**).

At the population level, we observe an abrupt rise in synchronization at E14.5 (**Fig. 5D**), quantified by the Kuramoto order parameter, where 0 denotes the absence of synchronization and 1 denotes complete synchronization. The abrupt shift in synchronization is also evident in spatial phase distributions at day 4 in culture (**Fig. 5E**), paralleling the abrupt synchronization emergence in the SCN (Carmona-Alcocer et al., 2018). These changes support the conclusion that the clock emergence process at both single-cell and population levels is not gradual but discretely staged in developmental epochs.

Discussion

Our study identifies the embryonic choroid plexus as the earliest detectable brain circadian clock that emerges before the SCN. Through PER2::LUC time-lapse recording in 4VCP explant cultures, we found that circadian PER2 rhythms appear at around E12, 2–3 days earlier than the master circadian clock. We also observed staged assembly of the transcriptional clock circuit, with a delayed rise of *Bmal1* transcripts, coincident with expression of differentiation markers. Accordingly, we detected the delayed onset of *Bmal1-ELuc* oscillations *ex vivo* around E13.5.

Circadian profiling across embryonic development revealed that 8 out of 12 clock genes exhibited at least transient circadian expression before E16.5 and displayed strong, developmentally shifting correlations with maternal clock genes. Between E11.5 and E13.5, coincident with placental maturation and the onset of maternal-fetal circulation, correlations among embryonic clock gene clusters were largely disrupted. Before full hemotrophic nutrition is established, the embryonic clock may be susceptible to blood-independent global cues such as temperature, consistent with SNIC-like sensitivity near onset. As the placenta matures, selective endocrine gating attenuates maternal influence, creating a developmental window for autonomous emergence and self-organization of embryonic circadian clocks.

The CP, the first clock in the brain?

Contrary to the prevailing assumption that the SCN is the primary structure to be circadian in the mouse embryo because of its crucial role in adulthood, we found that the 4VCP clock emerges earlier than the SCN. In our study, the 4VCP is the earliest brain structure to display clear circadian rhythmicity, though our search was limited to select sagittal sections rather than the entire three-dimensional embryonic brain. The 4VCP nevertheless has strong functional implications as the first clock, given our earlier demonstration that the adult 4VCP acts as a robust and influential oscillator capable of entraining the SCN both *ex vivo* and *in vivo* (Myung

et al., 2018). It is also notable that the first three structures we identified as circadian before or around E15.5 are the CP, SCN, and pituitary gland, which are all strategically positioned to regulate brain homeostasis, process external light cues, and propagate outputs through endocrine pathways. Strikingly, these three structures also show the strongest oscillations within the postnatal mouse brain (Myung et al., 2018).

The CSF-containing ventricles play a substantial role in early development; by E10.5–E11.5, the brain ventricle volume is ≥10% of the head volume, substantially bathing the developing brain (Aristizábal et al., 2013). This embryonic CSF is filled with morphogens and growth factors (Kaiser and Bryja, 2020; Saunders et al., 2023; Lun et al., 2015a,b), mostly secreted by the CP. If the embryonic CP secretome is released in a circadian manner, the neuroepithelium lining the large ventricles would receive temporally patterned cues. Some of these inputs modulate transcription factors in neural progenitors and influence fate decisions (Lamus et al., 2020; Lehtinen et al., 2011; Subashini et al., 2017). Although not circadian, oscillations of basic-helix-loop-helix (bHLH) factors such as *Hes1*, *Ascl1*, and *Olig2* promote cell proliferation, whereas sustained expression promotes cell differentiation (Imayoshi et al., 2013). By inhibiting differentiation, the progenitor pool can expand before neurogenesis begins, a prerequisite for reaching an appropriate number of both neurons and neural progenitors in the adult brain (Caviness et al., 1995; Kriegstein and Alvarez-Buylla, 2009; Imayoshi and Kageyama, 2014). Other signaling pathways such as *Wnt*, *Hedgehog*, and *Notch* induce oscillatory patterns of target-gene expression to regulate neural progenitor development (Imayoshi et al., 2014). This volume transmission from the CP is particularly important early in development, when synaptic circuits have yet to mature. Synaptogenesis in the visual cortex, for instance, begins late in gestation and matures postnatally (Li et al., 2010).

Clock and CP differentiation

The temporal convergence between 4VCP clock onset in culture and the start of the developmental program, as well as the delay in clock onset between the 4VCP and the LVCP, illustrate a requirement for differentiation before the clock can begin (Dan et al., 2020). These results agree with previous studies showing that induced pluripotent stem cells (iPSCs), embryonic stem cells (ESCs), and pluripotent stem cells (PSCs) lack a circadian clock, which emerges during differentiation (Yagita et al., 2010; Kowalska et al., 2010; Kaneko et al., 2023; Umemura et al., 2017).

However, despite a progenitor profile marked by predominant markers such as *Gli3* and *Ki67* (**Fig. 2**), we observed early circadian expression *in vivo* as early as E9.5 for *Cry2* when tissue was processed immediately after sampling (**fig. S7**, **S8**). This differs from whole-embryo analyses (Cao et al., 2022; Dolatshad et al., 2010) and underscores the need to evaluate clock gene rhythmicity in a tissue-specific manner. It is possible that some early rhythmic transcripts in the 4VCPs reflect maternally driven activity. Challenges remain in determining the

autonomous nature of such early gene oscillations, as the developing clock system may not conform to the adult model. For example, neonatal circadian clocks, including the *Cry1*$^{-/-}$;*Cry2*$^{-/-}$ SCN, deviate from the behavior expected under the canonical TTFL model (Ono et al., 2013).

Expression of *Per2* and *Bmal1* is typically antiphasic in the mature clock, since BMAL1-complexes drive *Per2* transcription, and after a delay due to translational and post-translational modifications, PER2-complexes repress transcription driven by BMAL1-complexes. In contrast, in our mRNA dataset, the two components do not co-emerge in the 4VCP, and in cultured explant recordings, *Bmal1-ELuc* starts circadian expression approximately 2 days after PER2::LUC. This highlights the possibility that the very first oscillation of the embryonic clock may be independent of circadian *Bmal1* expression. It is plausible that other E-box activators operate during the early developmental stage, that do not need to be circadian themselves, as non-rhythmic *Bmal1* overexpression can lead to circadian expression of *Per2* (Liu et al., 2008) and *Bmal1* itself (Padlom et al., 2022). These features may relate to SNIC-like behavior, which most TTFL models do not predict. Regardless of the exact mechanism, this early clock could be physiologically important; for example, metabolic rhythms in glucose uptake have been observed in undifferentiated stem cells even when core clock genes appear arrhythmic (Paulose et al., 2012).

Entrainment of the late embryonic clock

Multiple lines of evidence indicate a relatively autonomous clock by late gestation. In preterm infants, circadian-like rhythms in body temperature, heart rate, and rest-activity are detectable in the NICU (Bueno et al., 2016; Mirmiran et al., 1990; Mirmiran and Kok, 1991; Govindan et al., 2024), consistent with a late-developing endogenous clock. Pups born from dams with late SCN lesions do not show inter-pup desynchrony, unlike litters from early SCN-lesioned dams (Davis and Gorski, 1988; Jud and Albrecht, 2006). In preterm infants, one study reported that the 24 h sleep-wake rhythm appears earlier in preterm than in full-term infants (Guyer et al., 2015), although amplitude may be lower and phase may differ (e.g., inverted heart rate rhythm; Govindan et al., 2024). Such phase differences could arise from changes in external zeitgebers such as feeding schedules or from antenatal glucocorticoid exposure. Dexamethasone, routinely given in preterm care to reduce neonatal respiratory distress risk (McGoldrick et al., 2020), is also a potent circadian synchronizer that resets peripheral clocks (Balsalobre et al., 2000). In mice, maternal food restriction during and after pregnancy can shift offspring rhythms (Canaple et al., 2018). While ultradian temperature fluctuations in the NICU generally do not disrupt circadian development in infants born after mid-gestation (Thomas, 2001; Bueno et al., 2016; Mirmiran et al., 1990; Mirmiran and Kok, 1991), our data show that the 4VCP remains sensitive to weak (0.5 °C) temperature changes at E16, with reduced sensitivity by E18. These observations may help frame hypotheses about temperature-based care protocols tailored to developmental stages for preterm infants.

Conclusion

The early emergence of the circadian clock in the 4VCP from E11.5 to E12.5 challenges the long-held view of the SCN as the central player of the circadian pacemaking in the mammalian brain and, by extension, as the locus of developmental onset. Our findings also reveal that the onset is a discrete, multi-stage process. We show that the *ex vivo* rhythm of the canonical transcriptional activator *Bmal1* appears later than that of *Per2*, suggesting that the embryonic clock is not established by the classic BMAL1:CLOCK feedback. Instead, qPCR analysis of the embryonic 4VCP uncovered non-canonical rhythmic expression of *Rora* and *Rev-erbα* as early as E9.5. At the point of emergence, while mature circadian oscillators are often described by a Hopf bifurcation, we find that this transition shows hallmarks of a SNIC bifurcation. These insights imply two key consequences. First, the early clock in the 4VCP is well poised to guide the rhythms in other loci of the brain through the rhythmic secretion of factors into the CSF. Second, the internally multi-stage process and externally sudden emergence align with the idea that the circadian clock onset is a programmed developmental event, offering a new framework for understanding the maternal-fetal clock interactions and the potential impact of their disruption. By characterizing the precise timing, locus, and mechanism of the brain's first clock, our work provides insights into early circadian homeostasis that are highly relevant to preterm and neonatal settings.

Acknowledgements

We thank Lillian Byer for critical reading of the manuscript. This work was supported by the National Science and Technology Council (NSTC) (109-2314-B-038-071, 109-2320-B-038-020, 110-2314-B-038-162, 110-2311-B-038-003, 111-2314-B-038-008, 112-2314-B-038-063, 113-2314-B-038-121, 114-2320-B-038-052-MY3, 114-2811-B-038-015) and the Higher Education Sprout Project of the Ministry of Education (MOE) in Taiwan.

References

Abraham U, Granada AE, Westermark PO, Heine M, Kramer A, Herzel H (2010). Coupling governs entrainment range of circadian clocks. *Mol Syst Biol*, 6:438.

Alonso MI, Martín C, Carnicero E, Bueno D, Gato A (2011). Cerebrospinal fluid control of neurogenesis induced by retinoic acid during early brain development. *Dev Dyn*, 240:1650–1659.

Alonso MI, Lamus F, Carnicero E, Moro JA, de la Mano A, Fernández JMF, Desmond ME, Gato A (2017). Embryonic cerebrospinal fluid increases neurogenic activity in the brain ventricular-subventricular zone of adult mice. *Front Neuroanat*, 11:124.

Aristizábal O, Mamou J, Ketterling JA, Turnbull DH (2013). High-Throughput, High-Frequency 3-D Ultrasound for in Utero Analysis of Embryonic Mouse Brain Development. *Ultrasound Med Biol*, *39*:2321–2332.

Astiz M, Oster H (2021). Feto-maternal crosstalk in the development of the circadian clock system. *Front Neurosci*, 14:631687.

Awatramani R, Soriano P, Rodriguez C, Mai JJ, Dymecki SM (2003). Cryptic boundaries in roof plate and choroid plexus identified by intersectional gene activation. *Nat Genet*, 35:70–75.

Balsalobre A, Brown SA, Marcacci L, Tronche F, Kellendonk C, Reichardt HM, Schütz G, Schibler U (2000). Resetting of circadian time in peripheral tissues by glucocorticoid signaling. *Science*, 289:2344-2347.

Battogtokh D, Tyson JJ (2018). Deciphering the dynamics of interlocked feedback loops in a model of the mammalian circadian clock. *Biophys J*, 115:2055–2066.

Bedont JL, Blackshaw S (2015). Constructing the suprachiasmatic nucleus: a watchmaker's perspective on the central clockworks. *Front Syst Neurosci*, 9:74.

Birecree E, King LE, Nanney LB (1991). Epidermal growth factor and its receptor in the developing human nervous system. *Dev Brain Res*, 60:145–154.

Brown IR, Rush SJ (1996). In vivo activation of neural heat shock transcription factor HSF1 by a physiologically relevant increase in body temperature. *J Neurosci Res*, 44:52-57.

Brown RW, Diaz R, Robson AC, Kotelevtsev YV, Mullins JJ, Kaufman MH, Seckl JR (1996). The ontogeny of 11 beta-hydroxysteroid dehydrogenase type 2 and mineralocorticoid receptor gene expression reveal intricate control of glucocorticoid action in development. *Endocrinology*, 137:794–797.

Brown SA, Zumbrunn G, Fleury-Olela F, Preitner N, Schibler U (2002). Rhythms of mammalian body temperature can sustain peripheral circadian clocks. *Curr Biol*, 12:1574–1583.

Bueno C, Menna-Barreto L (2016). Development of sleep/wake, activity and temperature rhythms in newborns maintained in a neonatal intensive care unit and the impact of feeding schedules. *Infant Behav Dev*, 44:21–28.

Bueno D, Parvas M, Nabiuni M, Miyan J (2020). Embryonic cerebrospinal fluid formation and regulation. *Semin Cell Dev Biol*, 102:3–12.

Buhr ED, Yoo SH, Takahashi JS (2010). Temperature as a universal resetting cue for mammalian circadian oscillators. *Science*, 330:379–385.

Cai C, Vandermeer B, Khurana R, Nerenberg K, Featherstone R, Sebastianski M, Davenport MH (2019). The impact of occupational shift work and working hours during pregnancy on health outcomes: a systematic review and meta-analysis. Am J Obstet Gynecol, 221:563–576.

Canaple L, Gréchez-Cassiau A, Delaunay F, Dkhissi-Benyahya O, Samarut J (2018). Maternal eating behavior is a major synchronizer of fetal and postnatal peripheral clocks in mice. *Cell Mol Life Sci*, *75*:3991–4005.

Cao X, Yan Y, Luo X, Yang X, Cui H, Yang Y, Li H (2022). Analyses of the circadian clock genes expression in whole embryos and maternal major tissues of mice. *J Mol Histol*, 53:473–482.

Carmona-Alcocer V, Abel JH, Sun TC, Petzold LR, Doyle FJ, Simms CL, Herzog ED (2018). Ontogeny of circadian rhythms and synchrony in the suprachiasmatic nucleus. *J Neurosci*, 38:1326–1334.

Caviness VS, Takahashi T, Nowakowski RS (1995). Numbers, time and neocortical neuronogenesis: a general developmental and evolutionary model. *Trends Neurosci*, 18:379–383.

Čečmanová V, Houdek P, Šuchmanová K, Sládek M, Sumová A (2019). Development and entrainment of the fetal clock in the suprachiasmatic nuclei: the role of glucocorticoids. *J Biol Rhythms,* 34:307–322.

Chau KF, Springel MW, Broadbelt KG, Park HY, Topal S, Lun MP, Mullan H, Maynard T, Steen H, LaMantia AS, Lehtinen MK (2015). Progressive differentiation and instructive capacities of amniotic fluid and cerebrospinal fluid proteomes following neural tube closure. *Dev Cell*, 35:789–802.

Courtney Y, Head JP, Dani N, Chechneva OV, Shipley FB, Zhang Y, Holtzman MJ, Sadegh C, Libermann TA, Lehtinen MK (2025). Choroid plexus apocrine secretion shapes CSF proteome during mouse brain development. *Nat Neurosci*, 28:1446–1459.

Dan H, Ruan T, Sampogna RV (2020). Circadian clock regulation of developmental time in the kidney. *Cell Rep*, 31:107661.

Daubechies I, Lu J, Wu HT (2011). Synchrosqueezed wavelet transforms: An empirical mode decomposition-like tool. *Appl Comput Harmon Anal*, 30:243–261.

Davari MH, Naghshineh E, Mostaghaci M, Mirmohammadi SJ, Bahaloo M, Jafari A, Mehrparvar AH (2018). Shift work effects and pregnancy outcome: A historical cohort study. *J Family Reprod Health*, 12:84–88.

Davis FC, Gorski RA (1988). Development of hamster circadian rhythms: role of the maternal suprachiasmatic nucleus. *J Comp Physiol A*, 162:601–610.

Dolatshad H, Cary AJ, Davis FC (2010). Differential expression of the circadian clock in maternal and embryonic tissues of mice. *PLoS ONE*, 5:e9855.

Dziegielewska KM, Ek J, Habgood MD, Saunders NR (2001). Development of the choroid plexus. *Microsc Res Tech*, 52:5–20.

Edelbo BL, Andreassen SN, Steffensen AB, MacAulay N (2023). Day-night fluctuations in choroid plexus transcriptomics and cerebrospinal fluid metabolomics. *PNAS Nexus*, 2:pgad262.

Elmore SA, Cochran RZ, Bolon B, Lubeck B, Mahler B, Sabio D, Ward JM (2022). Histology atlas of the developing mouse placenta. *Toxicol Pathol*, 50:60–117.

Ermentrout B (1996). Type I membranes, phase resetting curves, and synchrony. *Neural Comput*, 8:979–1001.

Gato A, Moro JA, Alonso MI, Bueno D, de La Mano A, Martín C (2005). Embryonic cerebrospinal fluid regulates neuroepithelial survival, proliferation, and neurogenesis in chick embryos. *Anat Rec A Discov Mol Cell Evol Biol*, 284:475–484.

Gato A, Desmond ME (2009). Why the embryo still matters: CSF and the neuroepithelium as interdependent regulators of embryonic brain growth, morphogenesis and histiogenesis. *Dev Biol*, 327:263–272.

Govindan RB, Andescavage NN, Basu S, Murnick J, Ngwa J, Galla JT, Kapse K, Limperopoulos C, du Plessis A (2024). Circadian rhythm development in preterm infants: The role of postnatal versus postmenstrual age. *Early Hum Dev*, 196:106084.

Guyer C, Huber R, Fontijn J, Bucher HU, Nicolai H, Werner H, Molinari L, Latal B, Jenni OG (2015). Very preterm infants show earlier emergence of 24-hour sleep-wake rhythms compared to term infants. *Early Hum Dev*, 91:37–42.

Hildyard JCW, Wells DJ, Piercy RJ (2022). Identification of qPCR reference genes suitable for normalising gene expression in the developing mouse embryo. *Wellcome Open Res*, 6:197.

Huang X, Ketova T, Fleming JT, Wang H, Dey SK, Litingtung Y, Chiang C (2009). Sonic hedgehog signaling regulates a novel epithelial progenitor domain of the hindbrain choroid plexus. *Development*, 136:2535–2543.

Hunter NL, Dymecki SM (2007). Molecularly and temporally separable lineages form the hindbrain roof plate and contribute differentially to the choroid plexus. *Development*, 134:3449–3460.

Imayoshi I, Isomura A, Harima Y, Kawaguchi K, Kori H, Miyachi H, Fujiwara T, Ishidate F, Kageyama R (2013). Oscillatory control of factors determining multipotency and fate in mouse neural progenitors. *Science*, 342:1203–1208.

Imayoshi I, Kageyama R (2014). bHLH factors in self-renewal, multipotency, and fate choice of neural progenitor cells. *Neuron*, 82:9–23.

Jia BZ, Qi Y, Wong-Campos JD, Megason SG, Cohen AE (2023). A bioelectrical phase transition patterns the first vertebrate heartbeats. *Nature*, 622:149–155.

Johansson PA, Irmler M, Acampora D, Beckers J, Simeone A, Götz M (2013). The transcription factor Otx2 regulates choroid plexus development and function. *Development,* 140:1055–1066.

Jud C, Albrecht U (2006). Circadian rhythms in murine pups develop in absence of a functional maternal circadian clock. *J Biol Rhythms*, 21:149–154.

Kaiser K, Bryja V (2020). Choroid plexus: the orchestrator of long-range signalling within the CNS. *Int J Mol Sci,* 21:4760.

Kaneko H, Kaitsuka T, Tomizawa K (2023). Artificial induction of circadian rhythm by combining exogenous BMAL1 expression and polycomb repressive complex 2 inhibition in human induced pluripotent stem cells. *Cell Mol Life Sci*, 80:200.

Kowalska E, Moriggi E, Bauer C, Dibner C, Brown SA (2010). The circadian clock starts ticking at a developmentally early stage. *J Biol Rhythms*, 25:442–449.

Kriegstein A, Alvarez-Buylla A (2009). The glial nature of embryonic and adult neural stem cells. *Annu Rev Neurosci*, 32:149–184.

Lamus F, Martín C, Carnicero E, Moro JA, Fernández JMF, Mano A, Gato Á, Alonso MI (2020). FGF2/EGF contributes to brain neuroepithelial precursor proliferation and neurogenesis in rat embryos: the involvement of embryonic cerebrospinal fluid. *Dev Dyn*, 249:141–153.

Landgraf D, Koch CE, Oster H, Alvarez-Bolado G, Pombal MA (2014). Embryonic development of circadian clocks in the mammalian suprachiasmatic nuclei. *Front Neuroanat,* 8:143.

Langford MB, O'Leary CJ, Veeraval L, White A, Lanoue V, Cooper HM (2020). WNT5a regulates epithelial morphogenesis in the developing choroid plexus. *Cereb Cortex*, 30:3617–3631.

Lehtinen MK, Zappaterra MW, Chen X, Yang YJ, Hill AD, Lun M, Maynard T, Gonzalez D, Kim S, Ye P, D'Ercole AJ, Wong ET, LaMantia AS, Walsh CA (2011). The cerebrospinal fluid provides a proliferative niche for neural progenitor cells. *Neuron*, 69:893–905.

Li M, Cui Z, Niu Y, Liu B, Fan W, Yu D, Deng J (2010). Synaptogenesis in the developing mouse visual cortex. *Brain Res Bull*, 81:107–113.

Liu AC, Tran HG, Zhang EE, Priest AA, Welsh DK, Kay SA (2008). Redundant function of REV-ERBα and β and non-essential role for Bmal1 cycling in transcriptional regulation of intracellular circadian rhythms. *PLoS Ge*net, 4:e1000023.

Liška K, Sládek M, Čečmanová V, Sumová A (2021). Glucocorticoids reset circadian clock in choroid plexus via period genes. *J Endocrinol*, 248:155–166.

Lun MP, Johnson MB, Broadbelt KG, Watanabe M, Kang YJ, Chau KF, Springel MW, Malesz A, Sousa AMM, Pletikos M, Adelita T, Calicchio ML, Zhang Y, Holtzman MJ, Lidov HGW, Sestan N, Steen H, Monuki ES, Lehtinen MK (2015a). Spatially heterogeneous choroid plexus transcriptomes encode positional identity and contribute to regional CSF production. *J Neurosci*, 35:4903–4916.

Lun MP, Monuki ES, Lehtinen MK (2015b). Development and functions of the choroid plexus-cerebrospinal fluid system. *Nat Rev Neurosci*, 16:445–457.

Maeda Y, Muro M, Shono M, Shono H, Iwasaka T (2006). Diurnal rhythms in fetal heart rate baseline and sustained fetal tachycardia in twin pregnancy. *Early Hum Dev*, 82:637–644.

Martín C, Bueno D, Alonso MI, Moro JA, Callejo S, Parada C, Martín P, Carnicero E, Gato A (2006). FGF2 plays a key role in embryonic cerebrospinal fluid trophic properties over chick embryo neuroepithelial stem cells. *Dev Biol,* 297:402–416.

Martin C, Alonso MI, Santiago C, Moro JA, de la Mano A, Carretero R, Gato A (2009). Early embryonic brain development in rats requires the trophic influence of cerebrospinal fluid. *Int J Dev Neurosci*, 27:733–740.

Mirmiran M, Kok JH, de Kleine MJK, Koppe JG, Overdijk J, Witting W (1990). Circadian rhythms in preterm infants: a preliminary study. *Early Hum Dev*, 23:139–146.

Mirmiran M, Kok JH (1991). Circadian rhythms in early human development. *Early Hum Dev*, 26:121–128.

Miyan JA, Nabiyouni M, Zendah M (2003). Development of the brain: a vital role for cerebrospinal fluid. *Can J Physiol Pharmacol*, 81:317–328.

Murayama Y, Kori H, Oshima C, Kondo T, Iwasaki H, Ito H (2017). Low temperature nullifies the circadian clock in cyanobacteria through Hopf bifurcation. *Proc Natl Acad Sci USA*, 114:5641–5646.

Myung J, Hong S, Hatanaka F, Nakajima Y, De Schutter E, Takumi T (2012). Period coding of Bmal1 oscillators in the suprachiasmatic nucleus. *J Neurosci*, 32:8900–8918.

Myung J, Hong S, DeWoskin D, De Schutter E, Forger DB, Takumi T (2015). GABA-mediated repulsive coupling between circadian clock neurons in the SCN encodes seasonal time. *Proc Natl Acad Sci USA*, 112:E3920–E3929.

Myung J, Schmal C, Hong S, Tsukizawa Y, Rose P, Zhang Y, Holtzman MJ, De Schutter E, Herzel H, Takumi T (2018). The choroid plexus is an important circadian clock component. *Nat Commun*, 9:1–13.

Myung J (2024). Enhancing bioluminescence imaging of cultured tissue explants using optical telecompression. *Sensors*, 24:6041.

Myung J, Vitet H, Truong VH, Ananthasubramaniam B (2025). The role of the multiplicity of circadian clocks in mammalian systems. *Sleep Med*, 131:106518.

Nakajima Y, Yamazaki T, Nishii S, Noguchi T, Hoshino H, Niwa K, Viviani VR, Ohmiya Y (2010). Enhanced beetle luciferase for high-resolution bioluminescence imaging. *PLoS ONE*, 5:e10011.

Oates AC, Morelli LG, Ares S (2012). Patterning embryos with oscillations: structure, function and dynamics of the vertebrate segmentation clock. *Development*, 139:625–639.

Ono D, Honma S, Honma KI (2013). Cryptochromes are critical for the development of coherent circadian rhythms in the mouse suprachiasmatic nucleus. *Nat Commun*, 4:1666.

Padlom A, Ono D, Hamashima R, Furukawa Y, Yoshimura T, Nishiwaki-Ohkawa T (2022). Level of constitutively expressed BMAL1 affects the robustness of circadian oscillations. *Sci Re*p, 12:19519.

Parada C, Escolà-Gil JC, Bueno D (2008). Low-density lipoproteins from embryonic cerebrospinal fluid are required for neural differentiation. *J Neurosci Res*, 86:2674–2684.

McGoldrick E, Stewart F, Parker R, Dalziel SR (2020). Antenatal corticosteroids for accelerating fetal lung maturation for women at risk of preterm birth. *Cochrane Database Syst Rev*, 3:CD004454.

Parvas M, Parada C, Bueno D (2008). A blood-CSF barrier function controls embryonic CSF protein composition and homeostasis during early CNS development. *Dev Biol*, 321:51–63.

Paulose JK, Rucker EB, Cassone VM (2012). Toward the beginning of time: Circadian rhythms in metabolism precede rhythms in clock gene expression in mouse embryonic stem cells. *PLoS ONE*, 7:e49555.

Salvante KG, Milano K, Kliman HJ, Nepomnaschy PA (2017). Placental 11 β-hydroxysteroid dehydrogenase type 2 (11β-HSD2) expression very early during human pregnancy. *J Dev Orig Health Dis,* 8:149–154

Saunders NR, Dziegielewska KM, Fame RM, Lehtinen MK, Liddelow SA (2023). The choroid plexus: A missing link in our understanding of brain development and function. *Physiol Rev*, 103:919–956.

Serón-Ferré M, Mendez N, Abarzua-Catalan L, Vilches N, Valenzuela FJ, Reynolds HE, Llanos AJ, Rojas A, Valenzuela GJ, Torres-Farfan C (2012). Circadian rhythms in the fetus. *Mol Cell Endocrinol*, 349:68–75.

Smarr BL, Zucker I, Kriegsfeld LJ (2016). Detection of successful and unsuccessful pregnancies in mice within hours of pairing through frequency analysis of high temporal resolution core body temperature data. *PLoS ONE*, 11:e0160127.

Stauder AJ, Dickson PW, Aldred AR, Schreiber G, Mendelsohn FA, Hudson P (1986). Synthesis of transthyretin (pre-albumin) mRNA in choroid plexus epithelial cells, localized by in situ hybridization in rat brain. *J Histochem Cytochem*, 34:949–952.

Strogatz SH (2024). *Nonlinear Dynamics and Chaos: With Applications to Physics, Biology, Chemistry, and Engineering*. 3rd ed. New York: Chapman & Hall/CRC.

Subashini C, Dhanesh SB, Chen CM, Riya PA, Meera V, Divya TS, Kuruvilla R, Buttler K, James J (2017). Wnt5a is a crucial regulator of neurogenesis during cerebellum development. *Sci Rep*, 7:42523.

Takahashi JS (2017). Transcriptional architecture of the mammalian circadian clock. *Nat Rev Genet*, 18:164–179.

Thomas KA (2001). Biological rhythm development in preterm infants: does health status influence body temperature circadian rhythm? *Res Nurs Health*, 24:170–180.

Thompson A, Han VKM, Yang K (2002). Spatial and temporal patterns of expression of 11β-hydroxysteroid dehydrogenase types 1 and 2 messenger RNA and glucocorticoid receptor protein in the murine placenta and uterus during late pregnancy. *Biol Reprod*, 67:1708–1718.

Truong VH, Myung J (2023). LocoBox: Modular hardware and open-source software for circadian entrainment and behavioral monitoring in home cages. *Sensors*, 23:9469.

Ukai-Tadenuma M, Kasukawa T, Ueda HR (2008). Proof-by-synthesis of the transcriptional logic of mammalian circadian clocks. *Nat Cell Biol*, 10:1154–1163.

Umemura Y, Koike N, Ohashi M, Tsuchiya Y, Meng QJ, Minami Y, Hara M, Hisatomi M, Yagita K (2017). Involvement of posttranscriptional regulation of Clock in the emergence of circadian clock oscillation during mouse development. *Proc Natl Acad Sci USA*, 114:E7479–E7488.

VanDunk C, Hunter LA, Gray PA (2011). Development, maturation, and necessity of transcription factors in the mouse suprachiasmatic nucleus. *J Neurosci*, 31:6457–6467.

Wharfe MD, Mark PJ, Wyrwoll CS, Smith JT, Yap C, Clarke MW, Waddell BJ (2016). Pregnancy-induced adaptations of the central circadian clock and maternal glucocorticoids. *J Endocrinol*, 228:135–147.

Wong SD, Wright KP, Spencer RL, Vetter C, Hicks LM, Jenni OG, LeBourgeois MK (2022). Development of the circadian system in early life: maternal and environmental factors. *J Physiol Anthropol*, 41:22.

Wreschnig D, Dolatshad H, Davis FC (2014). Embryonic development of circadian oscillations in the mouse hypothalamus. *J Biol Rhythms*, 29:299–310.

Yagita K (2024). Emergence of the circadian clock oscillation during the developmental process in mammals. *Curr Opin Genet Dev*, 84:102152.

Yagita K, Horie K, Koinuma S, Nakamura W, Yamanaka I, Urasaki A, Shigeyoshi Y, Kawakami K, Shimada S, Takeda J, Uchiyama Y (2010). Development of the circadian oscillator during differentiation of mouse embryonic stem cells in vitro. *Proc Natl Acad Sci USA*, 107:3846–3851.

Yamazaki S, Numano R, Abe M, Hida A, Takahashi RI, Ueda M, Block GD, Sakaki Y, Menaker M, Tei H (2000). Resetting central and peripheral circadian oscillators in transgenic rats. *Science*, 288:682–685.

Yoo SH, Yamazaki S, Lowrey PL, Shimomura K, Ko CH, Buhr ED, Siepka SM, Hong HK, Oh WJ, Yoo OJ, Menaker M, Takahashi JS (2004). PERIOD2::LUCIFERASE real-time reporting of circadian dynamics reveals persistent circadian oscillations in mouse peripheral tissues. *Proc Natl Acad Sci USA*, 101:5339–5346.

Zappaterra MW, Lehtinen MK (2012). The cerebrospinal fluid: Regulator of neurogenesis, behavior, and beyond. *Cell Mol Life Sci*, 69:2863–2878.

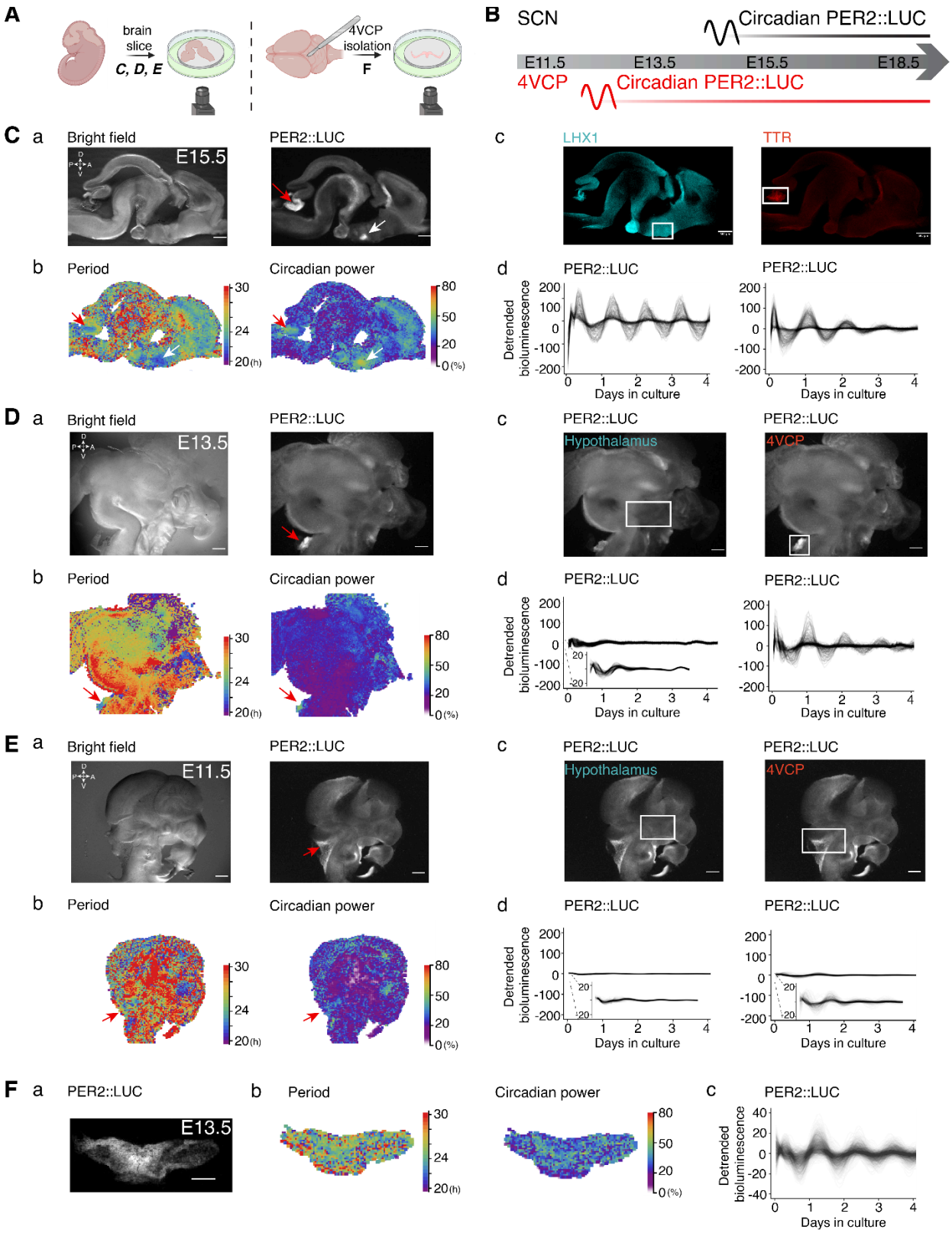

Figure 1. The 4VCP is circadian before the SCN in the mouse embryonic brain. (**A**) Workflow for recording PER2::LUC bioluminescence from embryonic brain/head slices (left; C-E) or from isolated

4VCP explants (right). (**B**) Developmental timeline summarizing that 4VCP PER2::LUC rhythms precede those in the SCN in the mouse embryo. (**C**) E15.5 brain slice. **a**: Bright-field (left) and bioluminescence (right) images; red arrow = 4VCP; white arrow = SCN. **b**: Maps of period (FFT-derived; left) and circadian power (percent ratio of power in the 24 ± 4 h band over the total 3–58 h band, see Materials and Methods; right). **c**: Post hoc immunofluorescence after tissue clearing confirms SCN (LHX1) (left) and choroid plexus (TTR) (right). **d**: Detrended PER2::LUC time series from the areas indicated by the white boxes in **Cc**; see **movie S1**. (**D**) E13.5 head slice. **a**: Bright-field and PER2::LUC images highlighting a rhythmic 4VCP (red arrow) and no SCN rhythm. **b**: Period (left) and circadian power (right) maps as in **Cb** (right). **c**: White boxes indicate the putative hypothalamus/SCN region (left) and 4VCP (right). **d**: Corresponding detrended time series; see **movie S2**. (**E**) E11.5 head slice. **a**: Bright-field and PER2::LUC images. **b**: Period (left) and circadian power (right) maps showing no robust circadian locus. **c**: White boxes indicate putative hypothalamus (left) and 4VCP (right). **d**: Flat detrended time series consistent with absent or weak rhythms at this stage; see **movie S3**. (**F**) Isolated E13.5 4VCP explant. **a**: PER2::LUC image. **b**: Period (left) and circadian power (right) maps. **c**: Detrended time series over 4 days; see **movie S4**. Scale bar: 500 μm. Red arrows indicate the 4VCP and white arrows indicate the SCN.

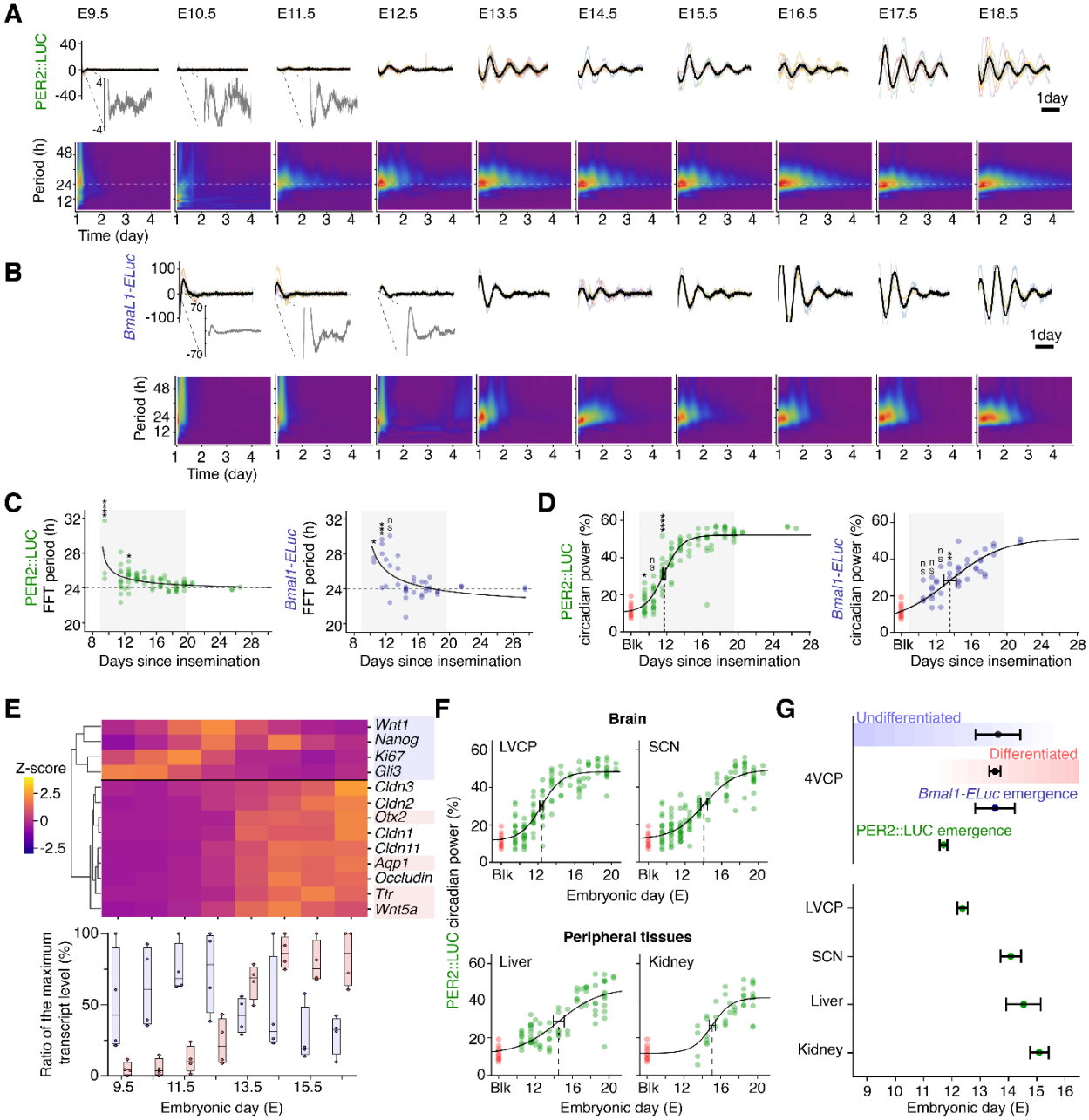

Figure 2. The 4VCP clock emerges at E11.5–E12.5, preceding the LVCP and the SCN, and coinciding with the onset of 4VCP differentiation. (**A**) Individual (thin colored) and mean (black) detrended traces (top) and spectrograms (bottom) of PER2::LUC bioluminescence recorded from embryonic 4VCP from E9.5 to E18.5. Zoom-in insets highlight low-amplitude rhythms. (**B**) Individual (thin colored) and mean (black) detrended traces (top) and spectrograms (bottom) of *Bmal1-ELuc* bioluminescence recorded from embryonic 4VCP from E10.5 to E18.5. Zoom-in insets highlight low-amplitude rhythms. (**C**) Period scatter plots for PER2::LUC (left) and *Bmal1-ELuc* (right) with $1/\sqrt{(t - t_0)}$ fits (consistent with SNIC). Significant difference from 24 h: one-way ANOVA followed by Tukey's post hoc analysis. *: $p < 0.05$, ***: $p < 0.001$, ****: $p < 0.0001$, ns: not significant. (**D**)

Circadian power scatter plots for PER2::LUC (left) and *Bmal1-ELuc* (right) with sigmoid fits versus embryonic age; emergence times (T_e) were E11.70 ± 0.14 and E13.52 ± 0.70, respectively (best fit estimate ± SE). Significant difference from 20%: one-way ANOVA with Tukey's post hoc. *: $p < 0.05$, **: $p < 0.01$, ****: $p < 0.0001$, ns: not significant. (**E**) Heat map of developmental-state marker genes (top) and box-and-whisker plots (bottom) comparing stem/progenitor markers (blue) and differentiation markers (red) in the 4VCP across embryonic stages; each gene is normalized to its maximum expression between E9.5 and E16.5. Each data point represents the mean of 5–15 litters (3–11 embryos per litter). Box-and-whiskers plot displays the minimum to maximum values, interquartile range (25th and 75th percentile), and median. (**F**) Developmental trajectories of circadian power for PER2::LUC oscillation in the LVCP and the SCN (upper panels) and liver and kidney (lower panels), overlaid with sigmoidal fits. (**G**) Comparison of the half-maximal times for progenitor markers (E13.63 ± 0.79), differentiation markers (E13.52 ± 0.20), and emergence time of *Bmal1-ELuc* and PER2::LUC oscillation in 4VCP, plus the PER2::LUC emergence time for each tissue.

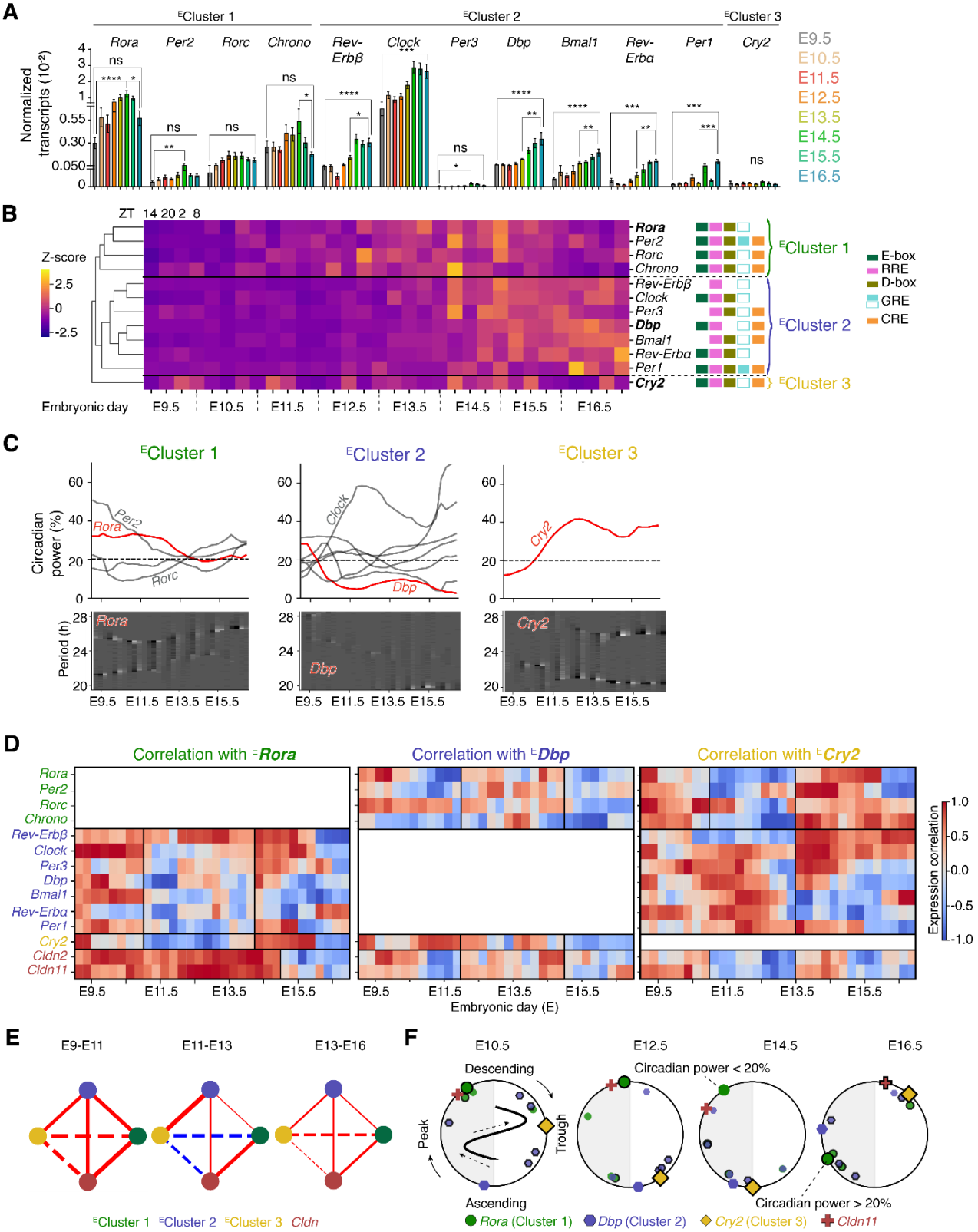

Figure 3. Expression patterns of clock genes in the embryonic 4VCP. (**A**) mRNA abundance of clock genes, normalized to the geometric mean of three internal reference genes (*Gapdh*, *Actb*, *Rpl13a*) across

embryonic stages E9–E16. Bars show the mean ± SEM of 8–20 litters (3–11 embryos per litter). One-way ANOVA with Tukey's post hoc test. *: $p < 0.05$, **: $p < 0.01$, ***: $p < 0.001$, ****: $p < 0.0001$, ns: not significant. (**B**) Hierarchical clustering and heat map of mRNA Z-scores across embryonic stages and ZT. Tiles on the right annotate promoter-motif classes (see **fig. S6A**). Each data point represents the mean of 2–5 litters (3–11 embryos per litter). (**C**) Circadian power for each embryonic clock gene, grouped by cluster (top; cluster-representative gene in red; dashed line, 20% detection threshold). Circadian phase-weighted power spectrogram for the representative gene of each cluster across embryonic days (bottom). (**D**) Heat maps of pairwise correlations between each embryonic gene and the cluster representative *Rora* (left), *Dbp* (middle), and *Cry2* (right). (**E**) Temporal correlation networks of embryonic genes. Nodes denote gene clusters; edge color and width encode sign and magnitude of mean Pearson correlation within each developmental window (blue negative, red positive; thicker edges indicate larger magnitude). Solid edges indicate correlations with consistent signs across stages; dashed edges indicate a sign change across stages. Black node outlines indicate genes with circadian power ≥ 20%. (**F**) Circular phase plots of embryonic gene expression across developmental stages. Each phase plot has 0 rad at 12 o'clock and increases clockwise. Representative genes are shown with larger opaque markers; non-representative genes are smaller and semi-transparent. Left-half shading indicates earlier phases. Marker shape and color indicate cluster membership; bold outlines highlight genes with circadian power ≥ 20%.

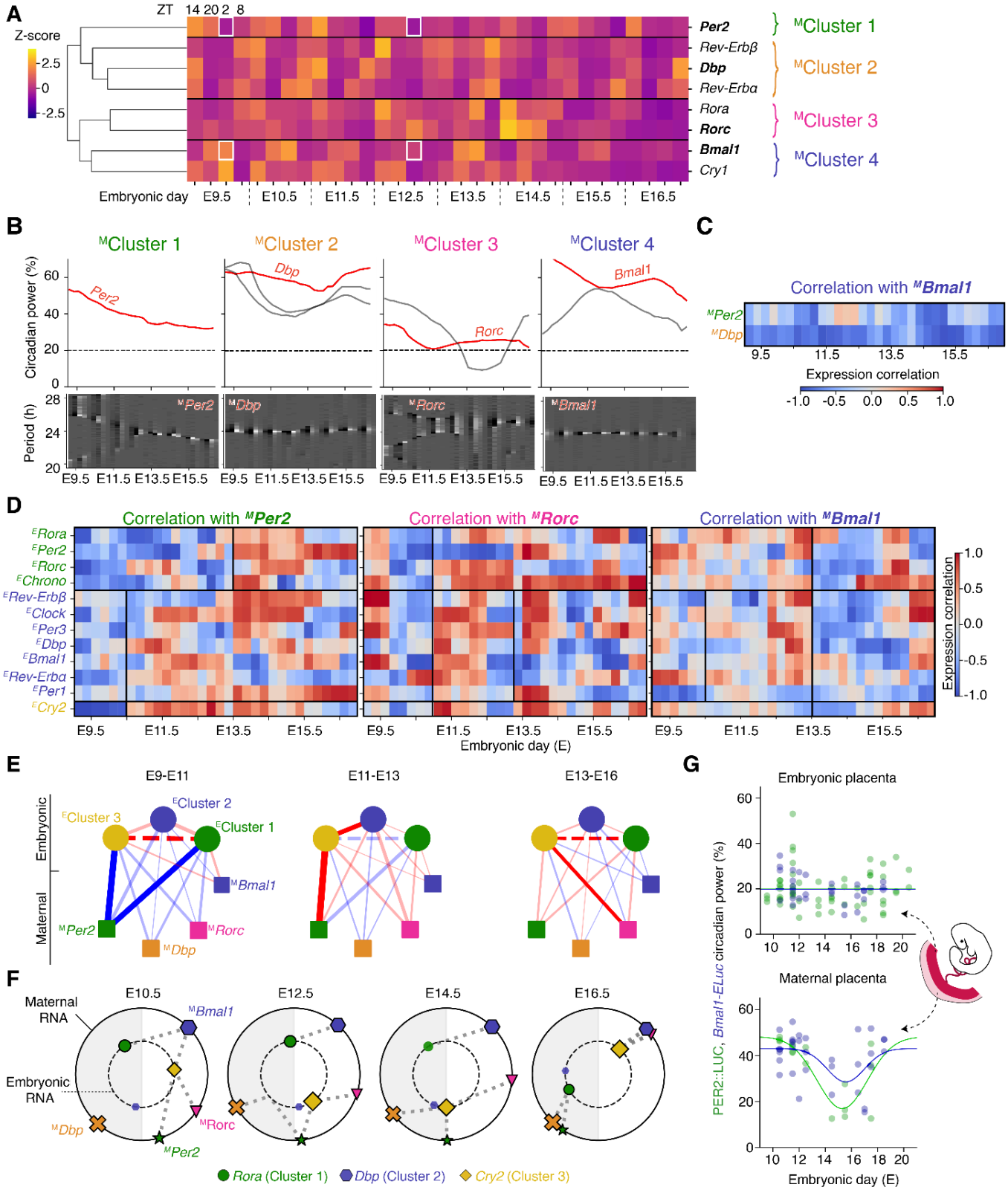
A
Z-score
2.5
0
-2.5
ZT 14 20 2 8
Per2
Rev-Erbβ
Dbp
Rev-Erbα
Rora
Rorc
Bmal1
Cry1
MCluster 1
MCluster 2
MCluster 3
MCluster 4
Embryonic day E9.5 E10.5 E11.5 E12.5 E13.5 E14.5 E15.5 E16.5
B
MCluster 1
MCluster 2
MCluster 3
MCluster 4
Circadian power (%)
Period (h)
Per2
Dbp
Rorc
Bmal1
E9.5 E11.5 E13.5 E15.5
C
Correlation with MBmal1
MPer2
MDbp
9.5 11.5 13.5 15.5
Expression correlation
-1.0 -0.5 0.0 0.5 1.0
D
Correlation with MPer2
Correlation with MRorc
Correlation with MBmal1
ERora
EPer2
ERorc
EChrono
ERev-Erbβ
EClock
EPer3
EDbp
EBmal1
ERev-Erbα
EPer1
ECry2
E9.5 E11.5 E13.5 E15.5
Embryonic day (E)
Expression correlation
1.0 0.5 0.0 -0.5 -1.0
E
E9-E11
E11-E13
E13-E16
Embryonic
Maternal
ECluster 3
ECluster 2
ECluster 1
MBmal1
MPer2
MRorc
MDbp
F
E10.5
E12.5
E14.5
E16.5
Maternal RNA
Embryonic RNA
MBmal1
MDbp
MRorc
MPer2
Rora (Cluster 1)
Dbp (Cluster 2)
Cry2 (Cluster 3)
G
Embryonic placenta
Maternal placenta
PER2::LUC, Bmal1-ELuc circadian power (%)
10 12 14 16 18 20
Embryonic day (E)

Figure 4. Maternal-embryonic transcriptional coordination reorganizes across embryonic development. (**A**) Hierarchical clustering and heat map of Z-scored mRNA for maternal clock genes across embryonic stages and ZT. Each data point represents the mean of 2–4 dams. White boxes highlight E9.5 ZT2 and E12.5 ZT2. (**B**) Circadian power trajectories for each maternal clock gene per cluster (top; cluster-representative gene in red; dashed line, 20% detection threshold). Circadian phase-weighted power spectrogram for the representative gene of each maternal gene cluster across embryonic days (bottom). (**C**) Heat map of pairwise correlations of maternal *Per2* and *Dbp* with maternal *Bmal1* across embryonic days. (**D**) Heat maps of correlation between each embryonic gene and maternal *Per2* (left), *Rorc* (middle), and *Bmal1* (right). (**E**) Temporal correlation networks summarizing maternal-embryonic gene expression correlations in three epochs (E9–11, E11–13, E13–16). Nodes are colored by embryonic clusters; edges show average Pearson correlation (red positive, blue negative, thickness indicates magnitude). Solid edges indicate consistent sign, dashed indicate changing sign. Black outlines mark genes with circadian power ≥ 20%. Only the top 30% strongest correlations are highlighted; others are semi-transparent gray. (**F**) Dual-radius phase plots of maternal and embryonic gene expression. Inner ring, embryonic cluster representatives; outer ring, selected maternal genes. Maternal-embryonic pairs are connected with dotted lines when both exhibit circadian power ≥ 20% and their phase difference is $< \pi/2$ rad (≤ 6 h). (**G**) PER2::LUC and *Bmal1-ELuc* circadian power in embryonic (top, dark pink; $n = 97$) and maternal (bottom, light pink; $n = 47$) placentas from E10.5 to E18.5; curves show inverted Gaussian fits.

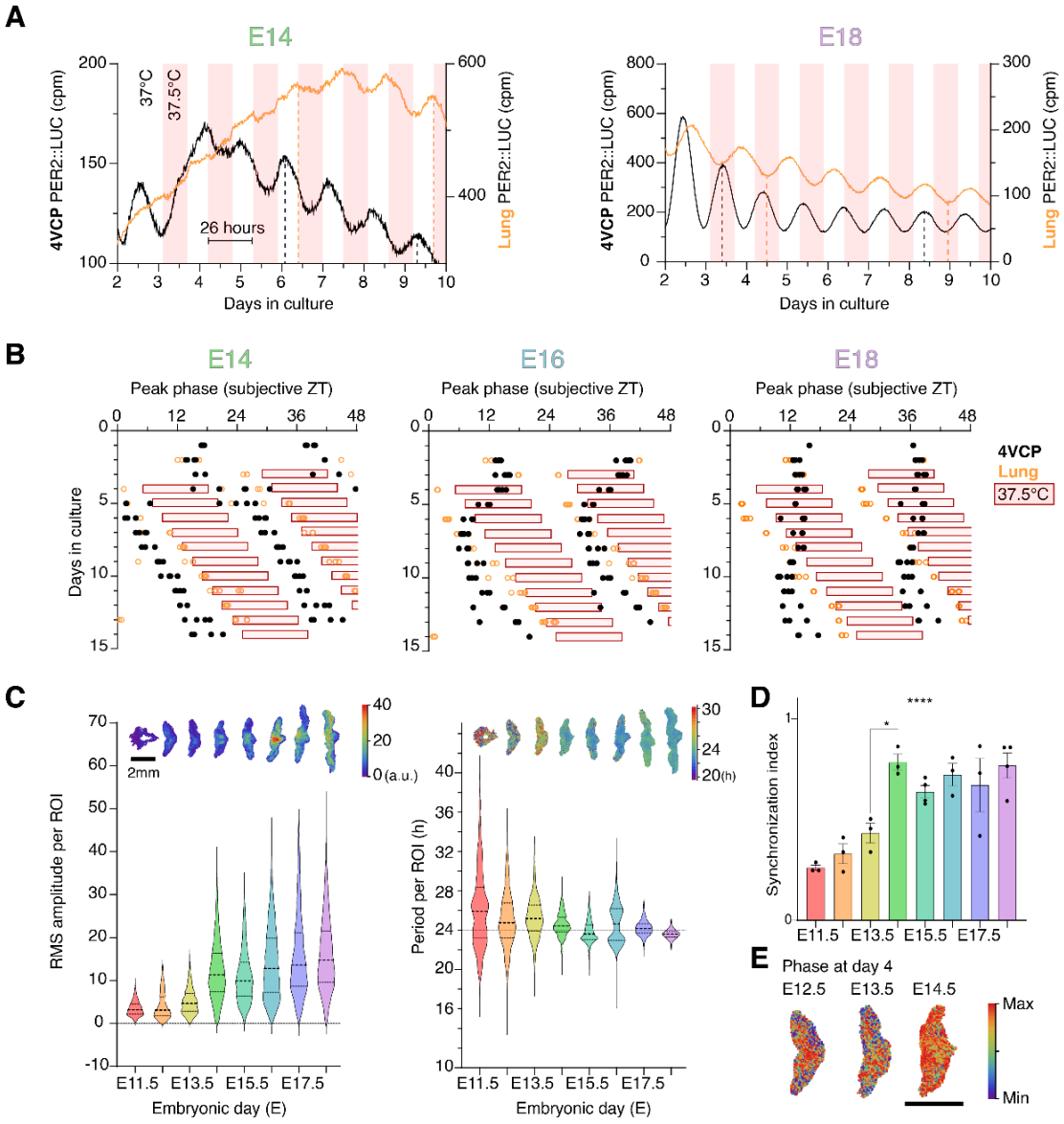

Figure 5. E14 and E16 4VCP, but not E18 4VCP, entrain to a weak 26-h period temperature cycle. (**A**) Raw PER2::LUC time series from 4VCP (black) and lung (orange) explanted at E14 (left) and E18 (right) for 12 days with a 0.5 °C square-wave cycle (26 h period) after 2 days at 37 °C. Red bars indicate the 37.5 °C epochs. (**B**) Double-plots of the peak phase of PER2::LUC time series from embryonic 4VCP (filled black circles) and lung (open orange circles) explants at E14 (left), E16 (middle), and E18 (right). Pale red boxes indicate the 37.5 °C epochs. (**C**) Single-cell analysis of embryonic 4VCP. Violin plots show single-cell ROI-level RMS amplitude (left) and period (right) from E11.5 to E18.5 (579–2,787 ROIs from 3–4 4VCP explants from 2–3 litters per stage). Dotted lines represent medians; solid black lines represent quartiles. Insets above each panel show representative amplitude (left) and period (right) maps across stages. (**D**) Synchronization index (Kuramoto order parameter, mean ± SEM) in embryonic 4VCP overlaid with scatter plots of individual

4VCP explants across stages (same *n* as in **C**). One-way ANOVA with Tukey's post hoc test; ****: $p < 0.0001$. (**E**) Representative 4VCP phase maps after 4 days in culture at E12.5, E13.5 and E14.5. Scale bar: 2 mm.

Supplementary Materials

	GenBank Accession	NCBI GeneID	Gene name	T_m (°C)	Primer sequence (5'-3')	Primer length
Genes used for normalization	NM_007393	11461	*Actb-c16X*, forward	64.6	GCCCTGAGGCTCTTTTCCAG	20
			Actb-c16X, reverse	63.8	TGCCACAGGATTCCATACCC	20
	NM_008084	14433	*Gapdh-4*, forward	62.6	AGGTCGGTGTGAACGGATTTG	21
			Gapdh-4, reverse	60.2	TGTAGACCATGTAGTTGAGGTCA	23
	NM_009438	22121	*Rpl13a*, forward	60.5	AGCCTACCAGAAAGTTTGCTTAC	23
			Rpl13a, reverse	61.0	GCTTCTTCTTCCGATAGTGCATC	23
4VCP positive genes	NM_008963	19215	*Ptgds*, forward	63.1	AATGGCTGCTCTTCGCATG	19
			Ptgds, reverse	64.8	GCCCCAGGAACTTGTCTTGTT	21
	NM_013697	22139	*Ttr*, forward	62.9	TTGCCTCGCTGGACTGGTA	19
			Ttr, reverse	61.8	TTACAGCCACGTCTACAGCAG	21
	NM_144841	18424	*Otx2*, forward	62.2	GAATCCAGGGTGCAGGTATGG	21
			Otx2, reverse	62.4	CTGAACTCACTTCCCGAGCTG	21
	NM_134110	246133	*Kcne2*, forward	60.8	CCACATTAGCCAATTTGACCCA	22
			Kcne2, reverse	62.4	CTCGGCTGTCGTGTTCCTC	19
4VCP negative genes	NM_008235	15205	*Hes1*, forward	62.2	CCAGCCAGTGTCAACACGA	19
			Hes1, reverse	61.0	AATGCCGGGAGCTATCTTTCT	21
	NM_010710	16870	*Lhx2*, forward	64.9	GCCGAGAAAGCGCAAGAGT	19
			Lhx2, reverse	64.3	TGTTCAGCATCGTTCTCGTTACA	23
	NM_008130	14634	*Gli3*, forward	62.4	CACAGCTCTACGGCGACTG	19
			Gli3, reverse	62.8	CTGCATAGTGATTGCGTTTCTTC	23
Clock genes	NM_007489	11865	*Bmal1*, forward	66.1	GCAGTGCCACTGACTACCAAGA	22
			Bmal1, reverse	62.8	TCCTGGACATTGCATTGCAT	20
	NM_011066	18627	*Per2*, forward	60.0	GAAAGCTGTCACCACCATAGAA	22
			Per2, reverse	60.5	AACTCGCACTTCCTTTTCAGG	21
	NM_007771	12952	*Cry1*, forward	64.7	AGAGGGCTAGGTCTTCTCGC	20
			Cry1, reverse	63.4	CTACAGCTCGGGACGTTCTC	20
	NM_007715	12753	*Clock*, forward	63.7	GTCCTTCAGCAGTCAGTCCAT	21
			Clock, reverse	63.7	GCCTCTATCATCCGTGTCCG	20
	NM_145434	217166	*Rev-erbα* (*Nr1d1*), forward	65.8	TGGCCTCAGGCTTCCACTATG	21
			Rev-erbα (*Nr1d1*), reverse	64.2	CCGTTGCTTCTCTCTCTTGGG	21
	NM_011584	353187	*Rev-erbβ* (*Nr1d2*), forward	61.8	CCCAAGAACGCTGATATCTCTAG	23
			Rev-erbβ (*Nr1d2*), reverse	62.1	ACACAGTAGAACCATGCCAC	20
	NM_013646	19883	*Rora*, forward	62.0	TCCAAATCCCACCTGGAAAC	20
			Rora, reverse	63.1	GGAAGGTCTGCCACGTTATCTG	22

	NM_011281	19885	*Rorc*, forward	60.6	TCCTGCCACCTTGAGTATAGTC	22
			Rorc, reverse	62.1	GTAAGTTGGCCGTCAGTGCTA	21
	NM_001352	1628	*Dbp*, forward	68.0	AATGACCTTTGAACCTGATCCCGCT	25
			Dbp, reverse	65.3	GCTCCAGTACTTCTCATCCTTCTGT	25
	NM_001033302	229599	*Chrono*, forward	61.6	GGAGACGAGTCTGAACACCC	20
			Chrono, reverse	62.4	GGGGCCGTATGAACCCTTG	19
	NM_009963	12953	*Cry2*, forward	64.2	GTCTGTGGGCATCAACCGA	19
			Cry2, reverse	64.3	TGCATCCCGTTCTTTCCCAA	20
	NM_001159367	18626	*Per1*, forward	62.6	CCCAGCTTTACCTGCAGAAG	20
			Per1, reverse	63.2	ATGGTCGAAAGGAAGCCTCT	20
	NM_011067	18628	*Per3*, forward	63.7	CACTTTGTCGACCTGCTTGC	20
			Per3, reverse	61.0	ATGAACCAAATAGGGGAGGAT	21
Tight junction genes	NM_016674	12737	*Cldn1*, forward	62.7	GGGGACAACATCGTGACCG	19
			Cldn1, reverse	61.1	AGGAGTCGAAGACTTTGCACT	21
	NM_016675	12738	*Cldn2*, forward	60.9	CAACTGGTGGGCTACATCCTA	21
			Cldn2, reverse	61.8	ATCCAGAGGCCCTTGGAAAAG	21
	NM_009902	12739	*Cldn3*, forward	62.3	ACCAACTGCGTACAAGACGAG	21
			Cldn3, reverse	62.6	CAGAGCCGCCAACAGGAAA	19
	NM_008770	18417	*Cldn11*, forward	62.1	ATGGTAGCCACTTGCCTTCAG	21
			Cldn11, reverse	61.2	AGTTCGTCCATTTTTCGGCAG	21
	NM_008756	18260	*Ocln*, forward	61.0	CTGGATCTATGTACGGCTCACA	22
			Ocln, reverse	61.1	TCCACGTAGAGACCAGTACCT	21
Development genes	NM_001256224	22418	*Wnt5a*, forward	62.6	CAACTGGCAGGACTTTCTCAA	21
			Wnt5a, reverse	63.7	CATCTCCGATGCCGGAACT	19
	NM_028016	71950	*Nanog*, forward	62.8	TCTTCCTGGTCCCCACAGTTT	21
			Nanog, reverse	60.1	GCAAGAATAGTTCTCGGGATGAA	23
	NM_001081117	17345	*Ki67*, forward	61.2	ATCATTGACCGCTCCTTTAGGT	22
			Ki67, reverse	62.0	GCTCGCCTTGATGGTTCCT	19
	NM_021279	22408	*Wnt1*, forward	60.4	GGTTTCTACTACGTTGCTACTGG	23
			Wnt1, reverse	62.3	GGAATCCGTCAACAGGTTCGT	21
	NM_007472	11826	*Aqp1*, forward	60.8	AGGCTTCAATTACCCACTGGA	21
			Aqp1, reverse	61.7	CTTTGGGCCAGAGTAGCGAT	20

Table S1. Primer sequences used for qPCR. T_m indicates melting temperature.

	E14	E16	E18	P0
4VCP	-1.83 ± 0.47 (*n* = 5)	-1.87 ± 0.70 (*n* = 4)	-1.82 ± 1.16 (*n* = 4)	2.86 ± 1.29 (*n* = 5)
SCN	-0.77 ± 0.76 (*n* = 5)	-1.3 ± 0.47 (*n* = 5)	-1.8 ± 1.05 (*n* = 5)	-0.93 ± 1.21 (*n* = 5)
LVCP	-1.03 ± 1.47 (*n* = 5)	-1.38 ± 1.44 (*n* = 5)	-0.46 ± 1.07 (*n* = 4)	-2.15 ± 1.09 (*n* = 5)
Lung	-0.02 ± 0.41 (*n* = 5)	-0.2 ± 0.3 (*n* = 5)	-0.34 ± 0.22 (*n* = 4)	-0.04 ± 0.54 (*n* = 5)

Table S2. Phase of entrainment (rad) under a 26 h temperature cycle. Shown are circular mean ± circular SD across 4–5 explants. For each explant, peak phase was averaged over the final 7 days of recording under the 26 h cycle (0 rad defined at the beginning of the 37.5 °C epoch; *n*: number of explants). Negative values indicate phase leading relative to 0 rad.

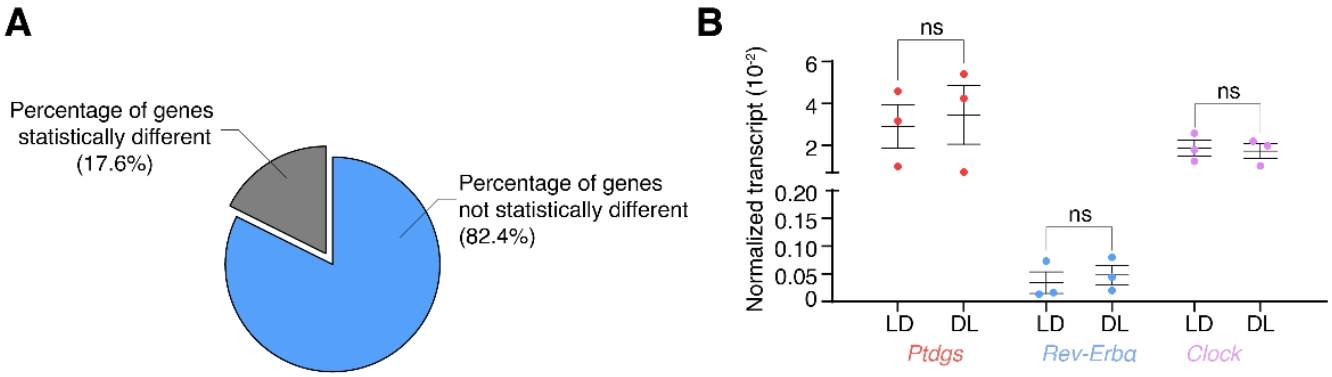

Figure S1. No overall statistical difference in mRNA expression between LD and DL protocols at E13.5. (**A**) 17 mRNA targets, including clock genes, were compared at 321 h postconception under LD (lights ON: 07:00, OFF: 19:00) and DL (lights ON: 22:00, OFF: 10:00) conditions. Most genes showed similar expression levels (82.4%), while 3 genes (17.6%; *Rora*, $p = 0.0108$; *Rev-erbβ*, $p = 0.0103$; *Cldn2*, $p = 0.0472$) showed significant differences by parametric *t*-test. (**B**) Representative expression levels of 3 genes (*Ptgds*, *Rev-erbα*, *Clock*), illustrating no significant differences between LD and DL in most cases. Parametric *t*-test; ns: not significant.

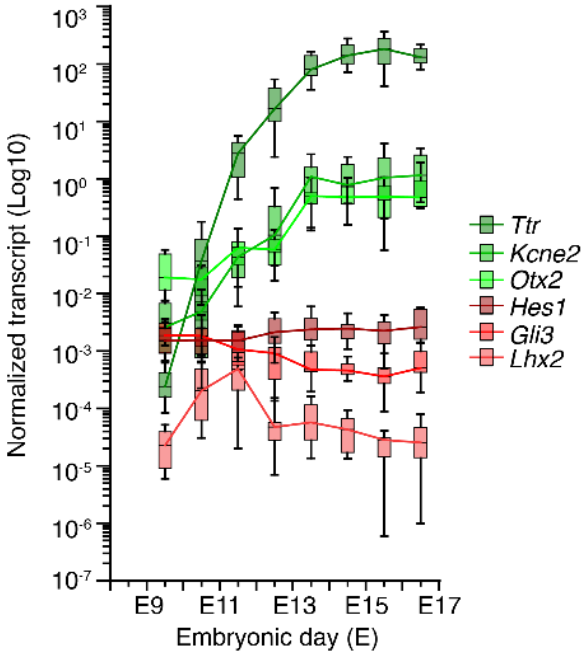

Figure S2. Molecular validation of the 4VCP dissection across embryonic stages. cDNA levels of selected 4VCP-positive (*Ttr*, *Kcne2*, *Otx2*) and 4VCP-negative (*Gli3*, *Lhx2*, *Hes1*) markers. At least 8 litters were analyzed per embryonic stage. Results are plotted on a $\log_{10}$ scale, with box-and-whisker plots showing the 10th-90th percentiles.

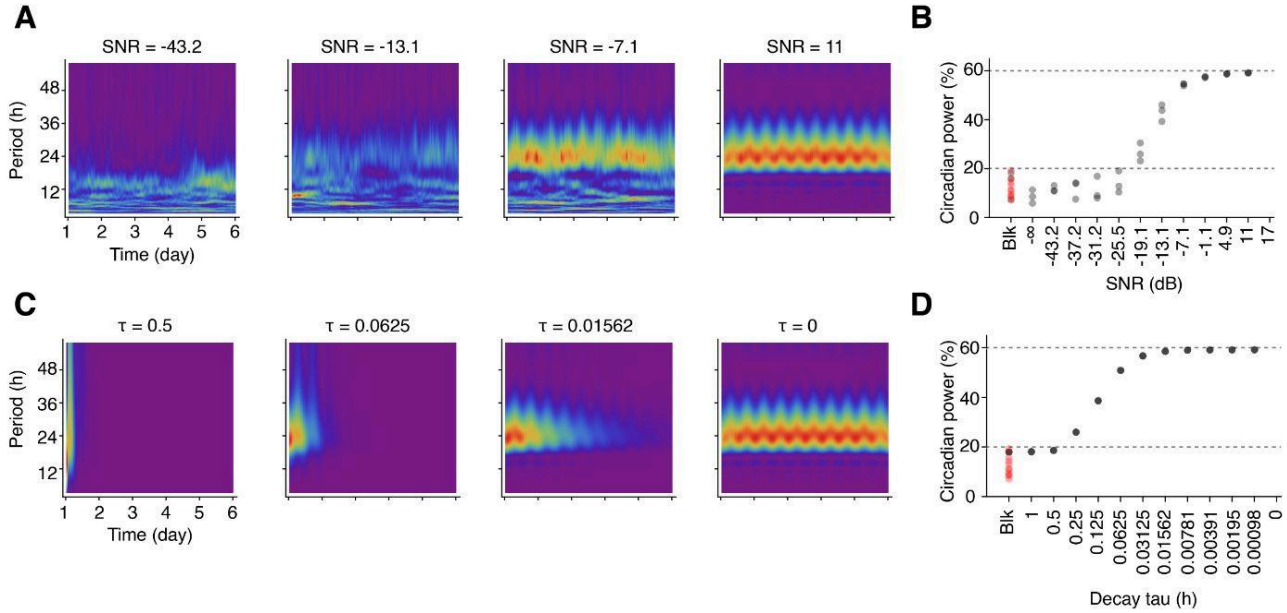

Figure S3. Quantification of circadian power in simulated bioluminescence reporter time series. (**A**) Power spectra from 2-day sliding-window fast Fourier transform (FFT) of simulated 24-h oscillations with varying relative noise amplitudes, expressed as signal-to-noise ratio (SNR, dB). Increasing SNR progressively reveals the circadian peak at ~24 h. (**B**) Circadian power as a function of SNR. Each point represents one simulation. Within this sliding window, detectable circadian rhythms range between 20% (detection threshold) to 60% (ceiling), marked by dashed lines. Blank recordings from experiments (Blk) fall below 20%. (**C**) Power spectra of simulated 24-h oscillations with different damping time constants (τ). Shorter τ produces stronger damping and loss of rhythmicity. (**D**) Circadian power as a function of τ. Although each semi-transparent point represents one simulation, they overlap substantially. As with SNR, non-detectable circadian rhythms fall below the 20% threshold (dashed line).

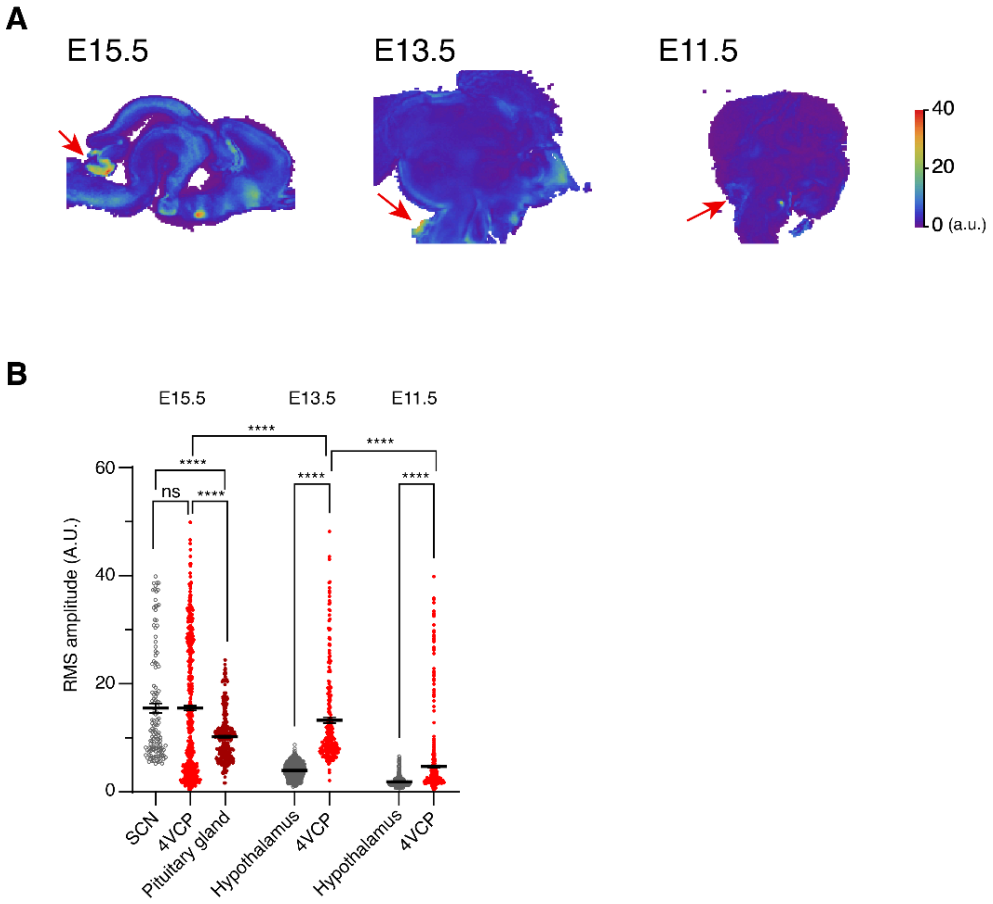

Figure S4. RMS amplitude of PER2::LUC in whole-brain slices at E15.5, E13.5, and E11.5. (**A**) Brain or head slices from E15.5 (left), E13.5 (middle) and E11.5 (right) embryos showing single-cell level RMS amplitude maps. A clear contrast in high RMS amplitude is visible in the 4VCP (red arrows), which becomes progressively more pronounced from E11.5 (right) to E15.5 (left). (**B**) RMS amplitude of each ROI by brain structure: SCN (or hypothalamus), 4VCP, and pituitary gland. One-way ANOVA followed by Tukey's post hoc analysis. ****: $p < 0.0001$, ns: not significant.

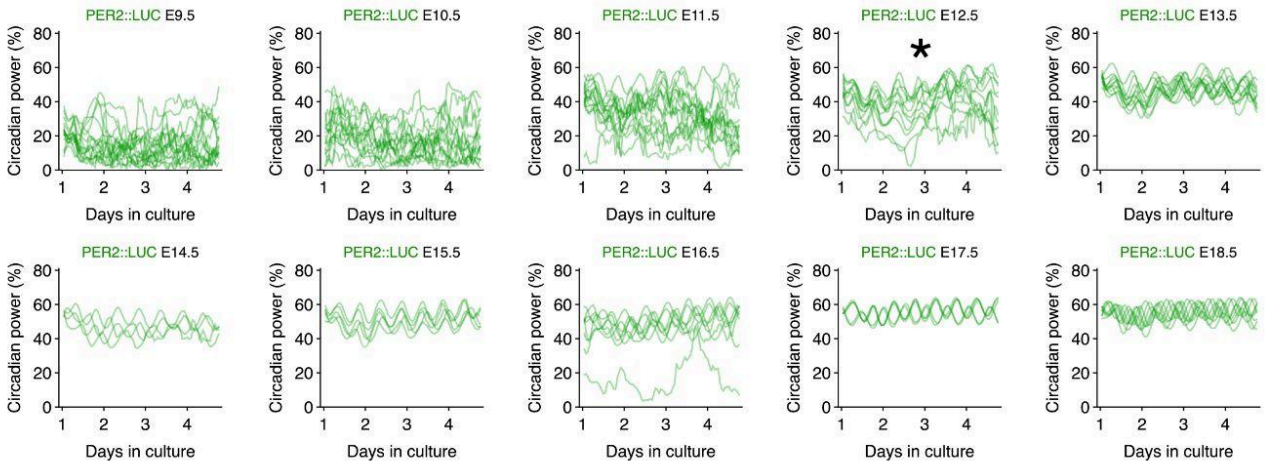

Figure S5. Abrupt emergence of PER2::LUC circadian power in 4VCP at E12.5. Circadian power of individual explants, with each line representing one explant, highlights the onset timepoint of the circadian rhythmicity. Circadian power was dispersed and mostly below 20% up to E10.5. At E11.5, circadian power remained variable, with some explants exceeding the 20% threshold but without consistent rhythmicity. At E12.5 (asterisk), circadian power shifted predominantly above 20%, marking the first embryonic stage of detectable circadian rhythms. From E13.5 onward, circadian power remained consistently elevated, approaching the ~60% ceiling during later stages (E14.5–E18.5).

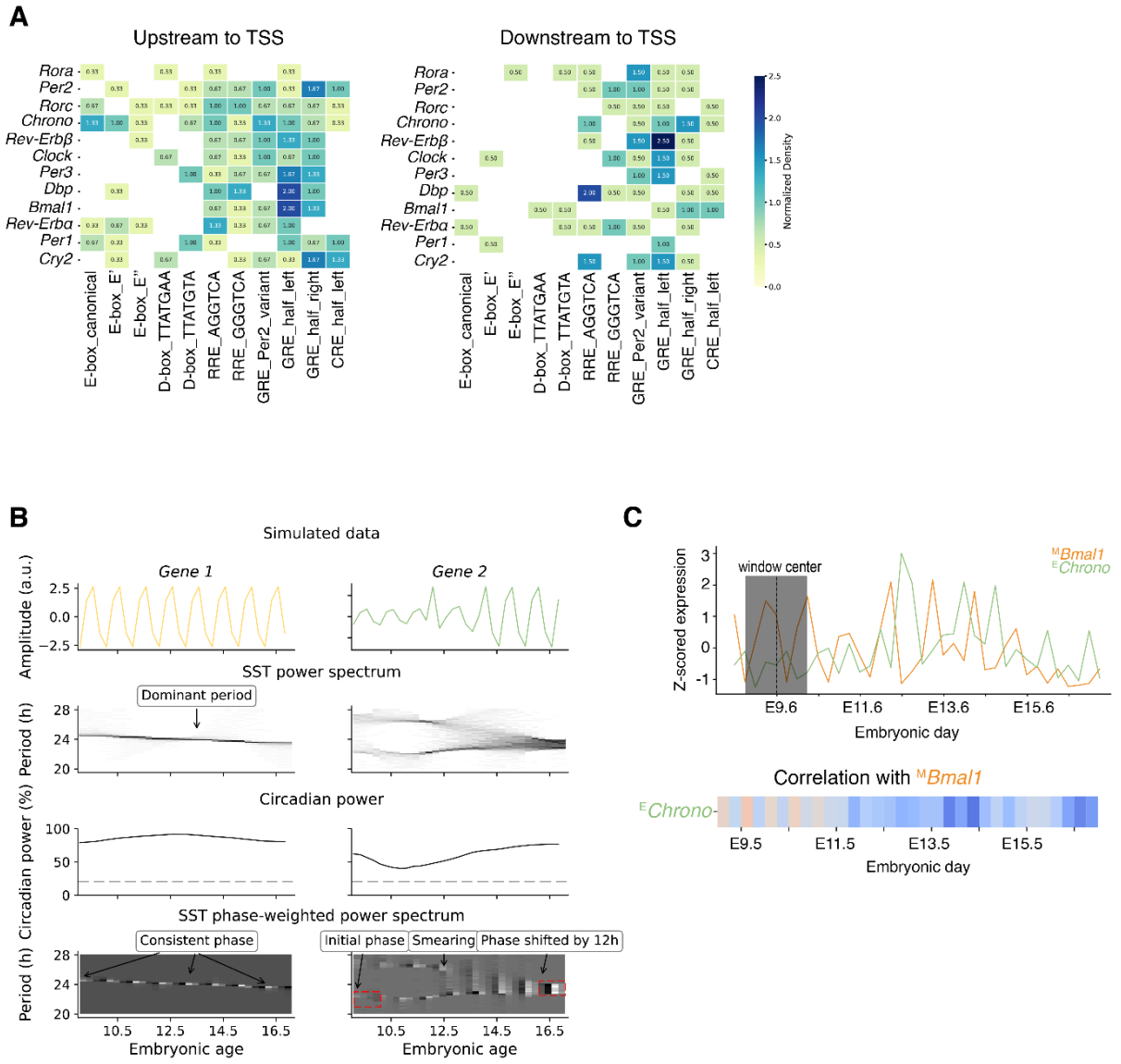

Figure S6. SST-CWT analysis of simulated data and maternal-embryonic correlation. (**A**) Normalized density map of motif counts within the 3 kb upstream and 2 kb downstream of the TSS of the indicated genes (see Materials and Methods). (**B**) SST-CWT analysis of simulated time series. (Top) Simulated bioluminescence signals for *Gene 1* (left) and *Gene 2* (right) over developmental time. *Gene 1* (maternal-like) maintains a stable amplitude and phase, while *Gene 2* (embryonic-like) undergoes amplitude changes and a 12 h phase shift. (Middle upper) SST-CWT power spectrograms highlighting dominant circadian periodicities between 20 and 28 h. (Middle) Circadian power of the two simulated genes. (Bottom) Phase-weighted SST-CWT power spectra, where color intensity reflects the consistency of the instantaneous phase of the dominant periods. Red dashed rectangles mark early (E9.5) and late (E16.5) windows used to illustrate phase reorganization during embryonic development. (**C**) Illustration of sliding-window correlation between maternal ^{M}*Bmal1* and embryonic ^{E}*Chrono* gene expression (top) and correlation of mRNA level between maternal ^{M}*Bmal1* and embryonic ^{E}*Chrono* in the 4VCP from E9.5 to E16.5 (bottom).

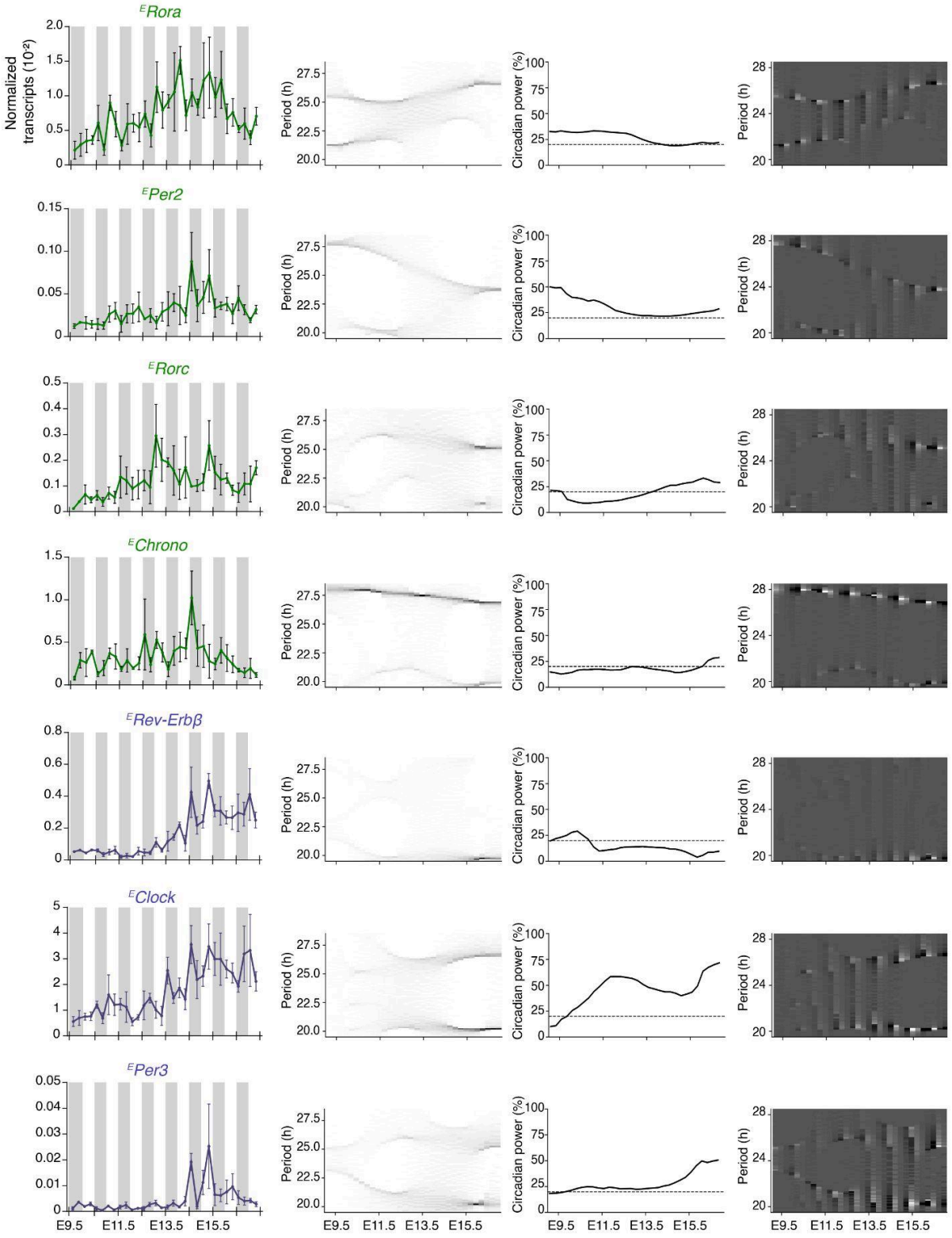

Figure S7. Circadian rhythmicity assessment of embryonic clock genes in the 4VCP. Each row corresponds to one clock gene in the embryonic 4VCP sampled every 6 h from

E9.5 to E16.5 (labels on the left). From left to right: (i) Raw mRNA expression level (mean ± SEM) across ZT2, ZT8, ZT14, ZT20, with gray shading indicating dark phase; (ii) SST-CWT power spectrograms highlighting dominant circadian periodicities between 20–28 h; (iii) Circadian power, with a 20% detection threshold shown as a dashed line; (iv) Phase-weighted SST-CWT power spectrogram that indicates both dominant period and circadian phase.

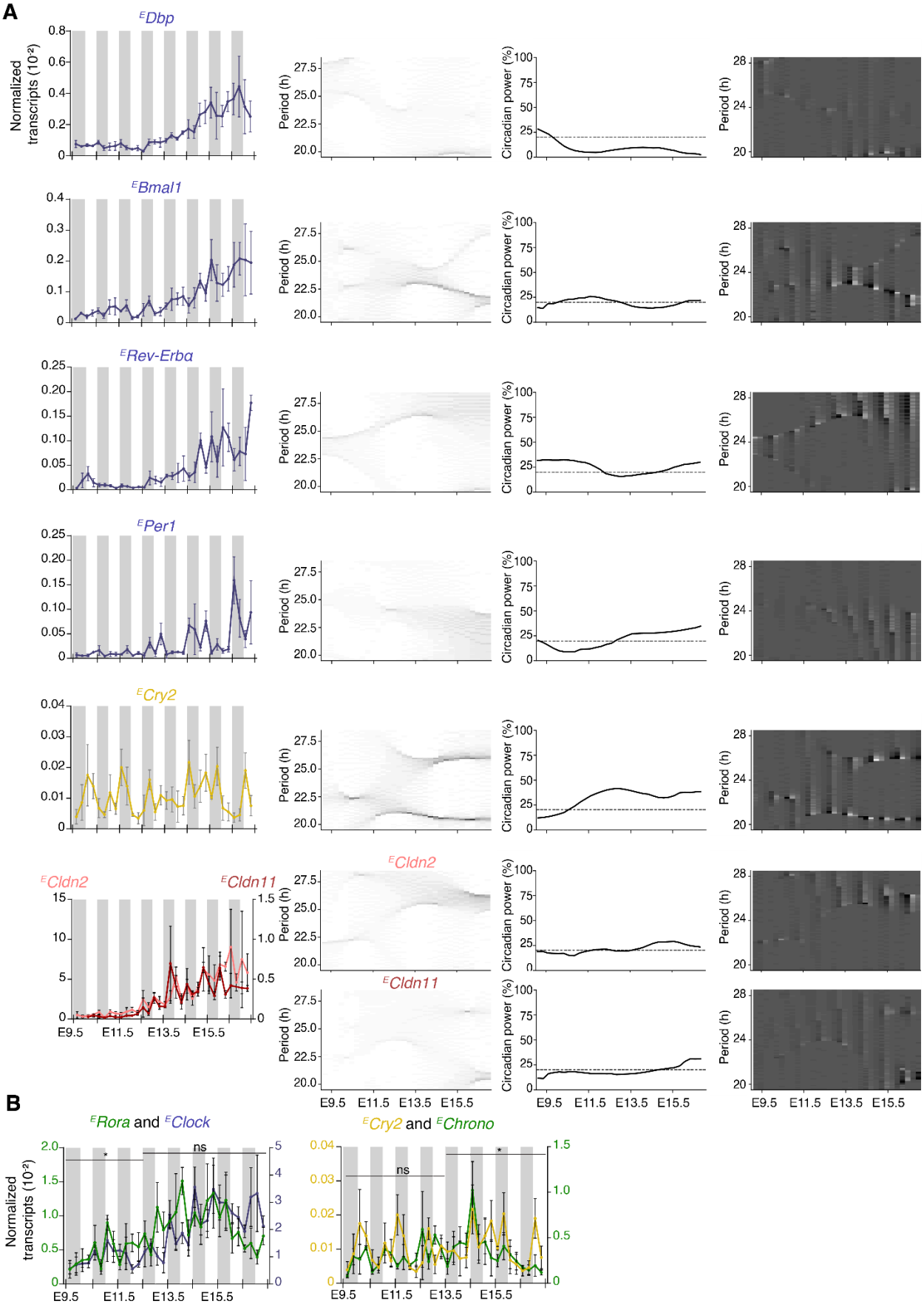
A
EDbp
EBmal1
ERev-Erbα
EPer1
ECry2
ECldn2
ECldn11
Normalized transcripts (10⁻²)
Period (h)
Circadian power (%)
E9.5
E11.5
E13.5
E15.5
B
ERora and EClock
ECry2 and EChrono
ns
*

Figure S8. Circadian rhythmicity and correlation of embryonic clock gene expression in the 4VCP. (**A**) Raw mRNA expression level (mean ± SEM) (leftmost), SST-CWT power spectrograms in the 20–28 h period bands (second from left), circadian power (third from left), and phase-weighted SST-CWT power spectrograms (rightmost) for clock genes of the embryonic 4VCP sampled every 6 h from E9.5 to E16.5. (**B**) Overlaid raw mRNA expression (mean ± SEM) for pairs of embryonic 4VCP clock genes: *Clock* and *Rora* (negatively correlated only between E11.5–E13.5) (left); *Cry2* and *Chrono* (positively correlated after E13.5) (right). Pearson correlation; *: $p < 0.05$, ns: not significant. Shaded regions denote the dark phase.

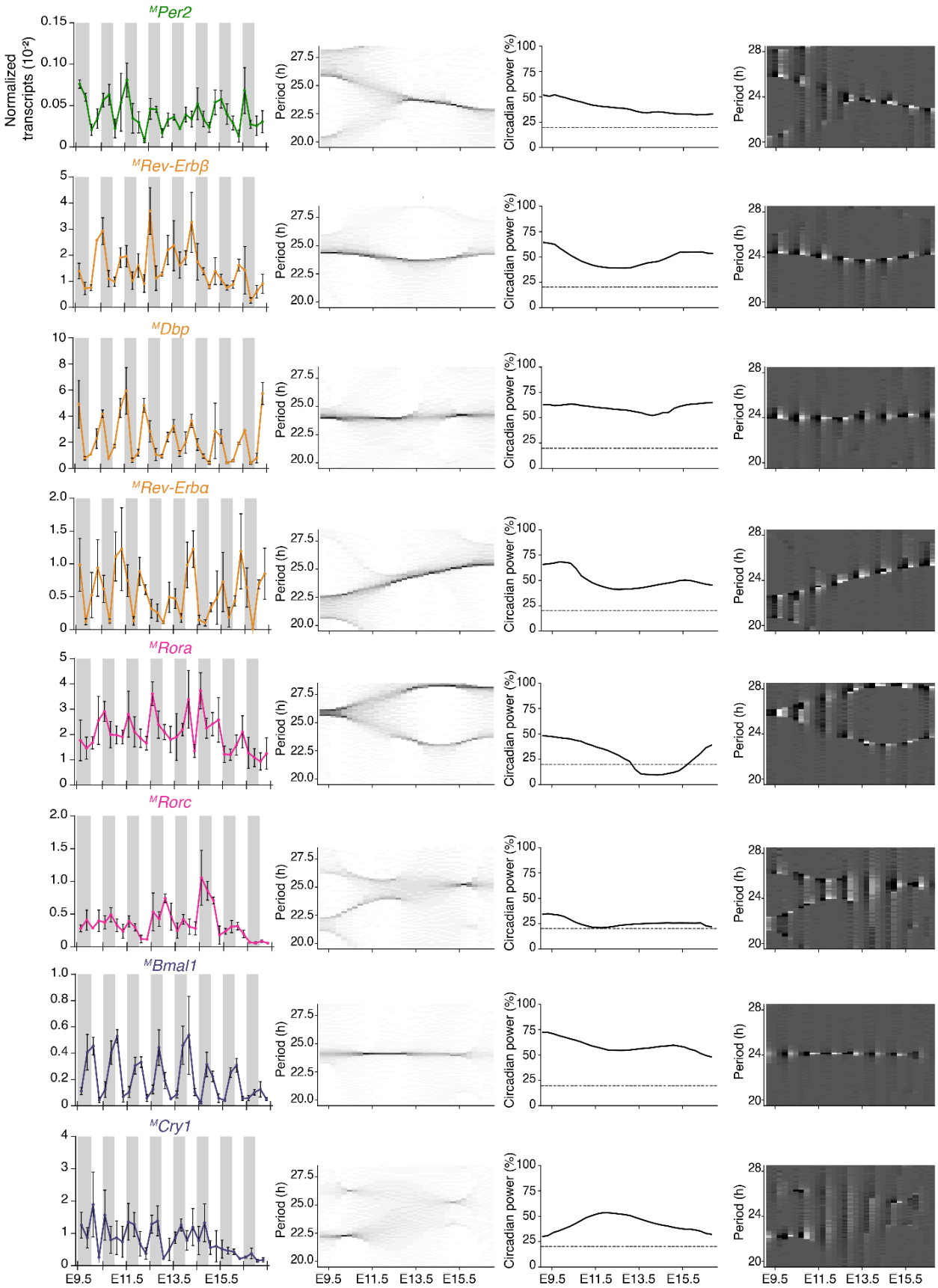
MPer2
MRev-Erbβ
MDbp
MRev-Erbα
MRora
MRorc
MBmal1
MCry1
Normalized transcripts (10-2)
Period (h)
Circadian power (%)
E9.5
E11.5
E13.5
E15.5

Figure S9. Circadian rhythmicity assessment of maternal clock genes in the 4VCP. From left to right: (i) Raw mRNA expression level (mean ± SEM) (leftmost); (ii) SST-CWT power spectrograms highlighting dominant circadian periodicities in the 20–28 h band; (iii) Circadian power, with a 20% detection threshold shown as a dashed line; (iv) Phase-weighted SST-CWT power spectrogram for clock genes of the maternal 4VCP sampled every 6 h from E9.5 to E16.5. All recordings were aligned to maternal ZT.

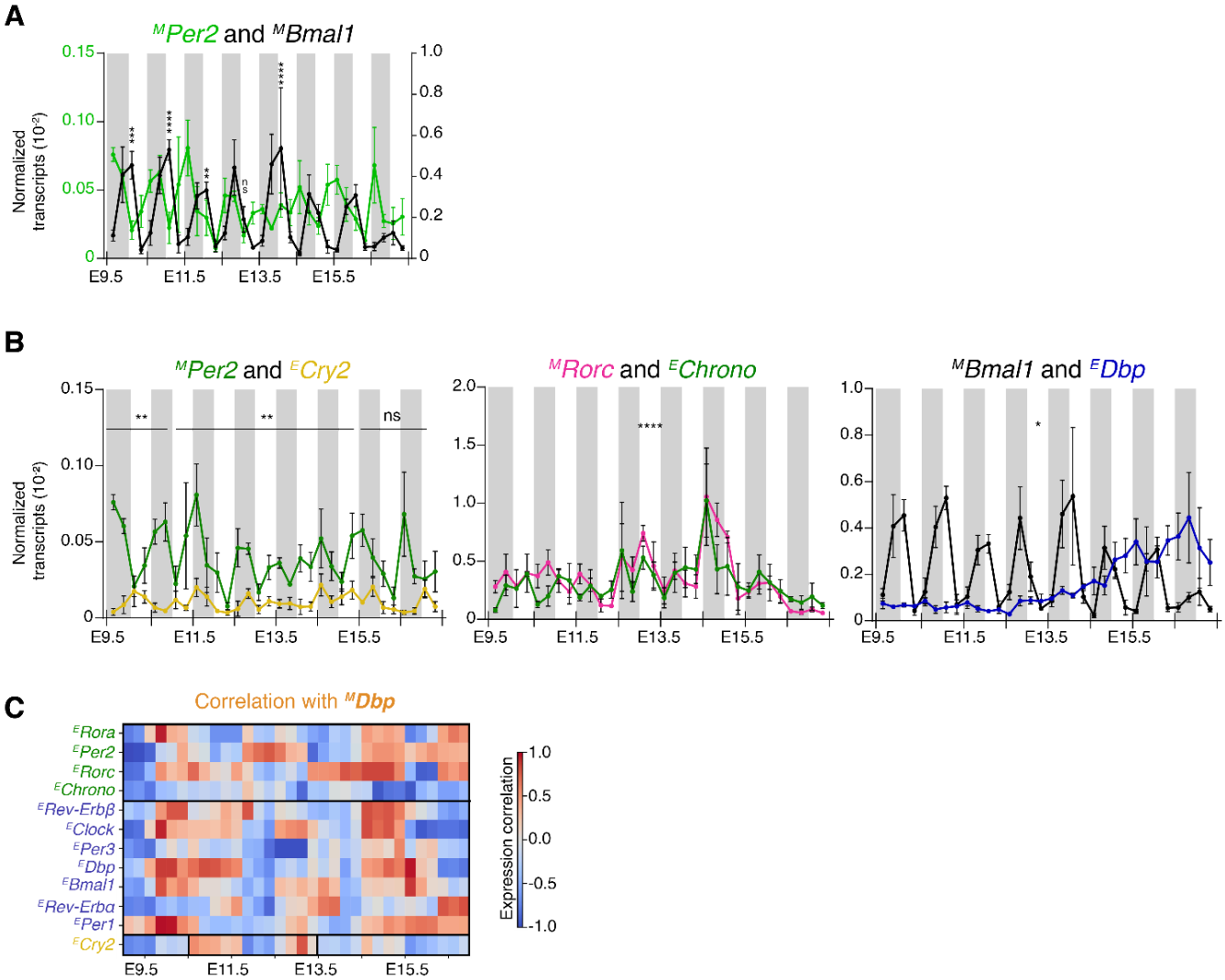

Figure S10. Raw data and correlations between maternal and embryonic clock gene expression in the 4VCP. (**A**) Overlaid raw mRNA expression (mean ± SEM) for maternal ^{M}*Per2* and ^{M}*Bmal1*, showing positive correlation (in-phase alignment) around E12.5–E13.5. Two-way ANOVA followed by Sidak's post hoc analysis. **: $p < 0.01$, ***: $p < 0.001$, ****: $p < 0.0001$, ns: not significant. (**B**) Overlaid raw mRNA expression (mean ± SEM) for maternal vs embryonic pairs: maternal ^{M}*Per2* vs embryonic ^{E}*Cry2* (strongly negatively correlated before E11.5) (left), maternal ^{M}*Rorc* vs embryonic ^{E}*Chrono* (positively correlated after E11.5) (middle), and maternal ^{M}*Bmal1* vs embryonic ^{E}*Dbp* (negatively correlated after E13.5). Pearson correlation; *: $p < 0.05$, **: $p < 0.01$, ****: $p < 0.0001$ ns: not significant (**C**) Heat maps of correlations between maternal ^{M}*Dbp*, representing Cluster 2 and embryonic clock genes.

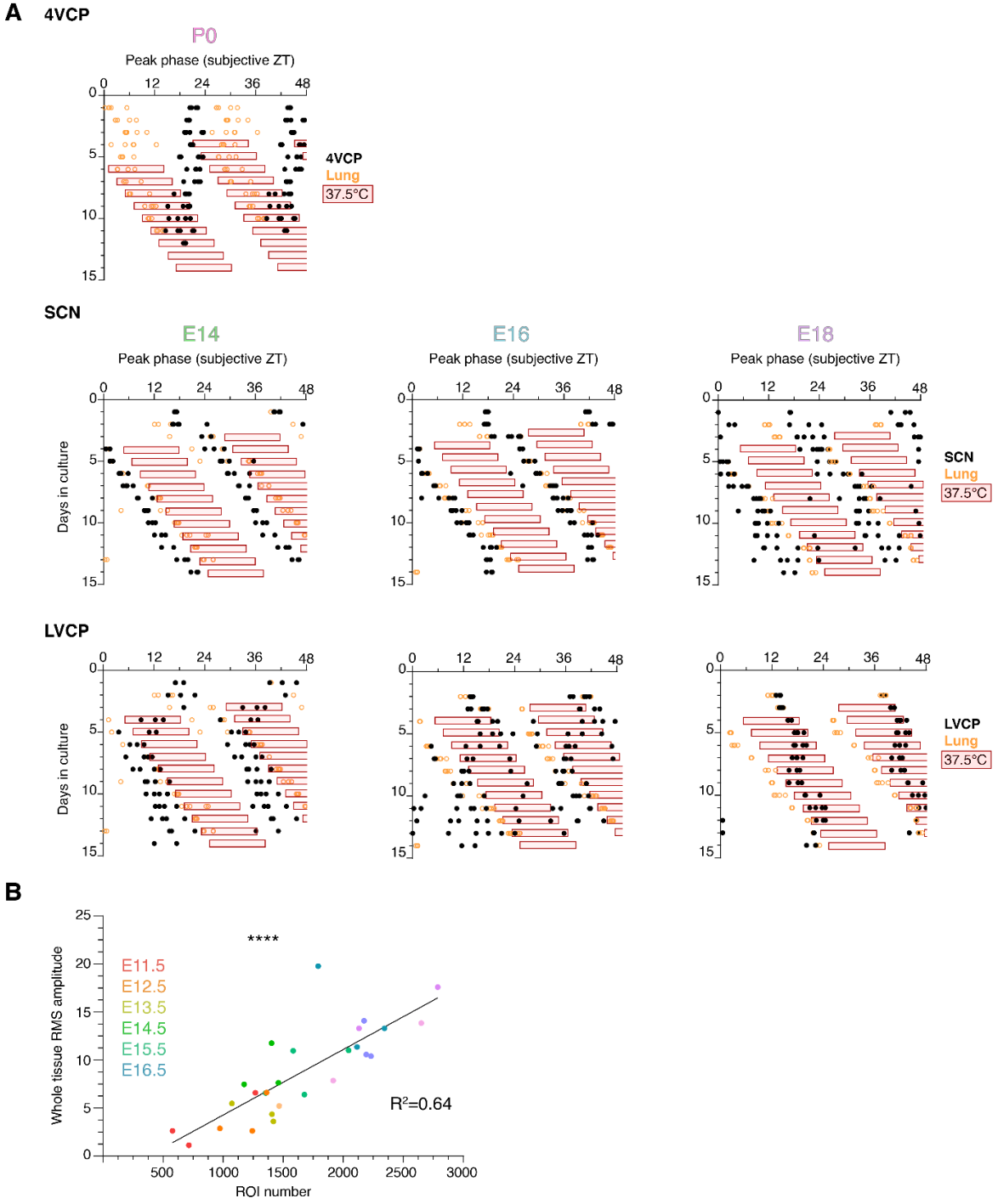

Figure S11. Sensitivity of embryonic SCN and LVCP to a 0.5 °C temperature cycle. (**A**) Double-plots of PER2::LUC peak phases from 3–5 neonatal 4VCPs at P0 (top row), SCNs (middle row) and embryonic LVCPs (bottom row) at E14, E16, and E18, over 12 days under a 0.5 °C, 26 h cycle after 2 days at 37.0 °C. In each panel, lung explants of the corresponding age are shown in orange as a reference. Red bars indicate the 37.5 °C

temperature epochs. (**B**) Linear correlation between whole-tissue RMS amplitude and the number of ROIs classified as cells in 4VCP across embryonic development (R^2 = 0.64; ****p < 0.0001). Line shows an ordinary least squares fit.

Supplementary Movies

Movie S1. Time-lapse of PER2::LUC in an E15.5 sagittal brain slice. Circadian rhythms are detected in the SCN and the 4VCP. Elapsed time (h) appears in the upper left. Scale bar: 500 μm.

Movie S2. Time-lapse of PER2::LUC in an E13.5 sagittal head slice. A circadian rhythm is detected only in the 4VCP. Elapsed time (h) appears in the upper left. Scale bar: 500 μm.

Movie S3. Time-lapse of PER2::LUC in an E11.5 sagittal head slice. PER2::LUC signal is present in the 4VCP, but no reliable circadian PER2::LUC rhythm is detected. Elapsed time (h) appears in the upper left. Scale bar: 500 μm.

Movie S4. Time-lapse of PER2::LUC in an isolated E13.5 4VCP explant. An endogenous circadian rhythm is evident *ex vivo*. Elapsed time (h) appears in the upper left. Scale bar: 500 μm.